Single Input Single Output Digital Pre-Distortion at Millimeter Wave Frequencies for Phased Arrays

by

Ahmed Ben Ayed

A thesis
presented to the University of Waterloo
in fulfillment of the
thesis requirement for the degree of
Master of Applied Science
in
Electrical and Computer Engineering

Waterloo, Ontario, Canada, 2019

I hereby declare that I am the sole author of this thesis. This is a true copy of the thesis, including any required final revisions, as accepted by my examiners.

I understand that my thesis may be made electronically available to the public.

Abstract

The limiting fact that is impeding the increase in data rate in the current generation of wireless communication is the limited available spectrum in the sub-6 GHz bands. This has motivated the shift to higher frequencies such as millimeter waves (mm-wave) and terahertz frequencies where modulation bandwidth of several hundreds of MHz can be utilized to increase the communication link capacity. The deployment of high data rate mm-wave base stations will highly depend on the maximum achievable equivalent isotropic radiated power (EIRP) and on the ability to generate reliable and error free wideband signals. High EIRP and high efficiency operation can be achieved by using active phased arrays operated deep into the power amplifiers (PAs) nonlinear region. In this work, a low power and low complexity compensation schemes to mitigate the impairments exhibited by phase arrays driven with wideband signals and high efficient nonlinear PAs at mm-wave frequencies are proposed.

Digital pre-distortion (DPD) techniques can provide an attractive solution to linearize high efficiency and high EIRP nonlinear phased arrays at mm-wave frequencies. However, the viable deployment of DPD solutions call for the reduction in the power consumption of the transmitter observation receiver (TOR) feedback path required to train the DPD function. To that end, a low power DPD scheme for linearizing mm-wave hybrid beamforming antenna systems is presented. The proposed DPD scheme exploits the modularity of hybrid beamforming systems. During the training phase, the constituent sub-arrays, are categorized, into (i) the main sub-array that exhibits non-linear distortion and is to be linearized, and (ii) the auxiliary sub-arrays that operate in the backoff region to avoid nonlinearity. To produce the error signal necessary to train the DPD function (and compensate for the distortions exhibited by the main sub-array), the signals transmitted by the main and auxiliary sub-arrays are combined. This error signal is captured using a TOR with low dynamic range and is digitized using a low-bit resolution analog-to-digital converter (ADC). Proof-of-concept validation experiments are conducted by applying the proposed DPD system to linearize an off-the-shelf hybrid-beamforming array comprised of four 64-element sub-arrays, operating at 28 GHz and driven with up to 800 MHz orthogonal frequency-division multiplexing (OFDM) modulated signals. Using the proposed DPD

scheme, a TOR with a 4-bit ADC was sufficient to improve the adjacent channel power ratio (ACPR) by 10 dB and the error vector magnitude (EVM) improved from 5.8% to 1.6%. These results are similar to those obtained using a TOR with 16-bit ADCs.

Reducing the complexity of the DPD scheme for phased arrays is also of primordial importance to the successful deployment of DPD solutions. For instance, the DPD function needs to be desensitize to the load modulation effects exhibited by large antenna systems and be able to linearize phased arrays at different steering angles. To address the challenges associated with the load modulation for phased arrays, we propose a generalized SISO DPD scheme as solution to minimize the EVM variation at different steering angles. The measurement results of the proposed scheme, using a 400 MHz OFDM signal with subcarriers modulated using 256 QAM and on a commercial 64-elements beamforming array, was able to maintain the EVM below 2% across the full steering range. This solution, however, failed to maintain the ACPR below -45 dBc. The effect of tapering on the load modulation and the array nonlinearity is also analysed. The measurement results using different tapers are used to validate the theory and the simulation results. Using tapering, the ACPR and EVM variation before and after DPD were minimized versus steering angles. For instance, using taper setting 2, the ACPR and EVM are maintained below -46 dBc and 1% from $-38°$ to $45°$ and below -42.3 dBc and 1.8% from $-45°$ to $45°$ respectively. Better results are measured when tapering is used in conjunction with the proposed generalized DPD scheme. In that case, the ACPR is improved from -35.5 to at worst -46.4 dBc and at best -50 dBc and the EVM is improved from at worst 4.5% to at worst 1.2% and at best 0.85%. The EVM is also maintained below 0.95% from $-39°$ to $45°$.

Acknowledgements

I would like to thank my supervisors Professor Slim Boumaiza and Professor Patrick Mitran for providing me with their guidance in this research work and the opportunity to take part in the research activities of the Emerging Radio System Group (EmRG).

Thank you to all my fellow EmRG lab member of their mentorship, encouragement and discussions in the office and in the laboratory.

Last but not least, I would like to thank my family for their constant support and love and Special thanks to Kraran, Varuna, Abeer, Sonya and Giovanni for always being their for me.

Table of Contents

List of Figures

Chapter 1

Introduction

Since the digital revolution and the industry paradigm shift to the information technology economy, the requirements for higher values of information transfer have been growing exponentially. In fact, according to the International Data Corporation (IDC), it is estimated that more than 150 billion devices will be connected across the globe by 2025 [6]. Moreover, Cisco's Visual Networking Index (VNI) predicts an overall increase in the Compound Annual Growth Rate (CAGR) of mobile data traffic by 46% between 2017 and 2022 [7]. This rapid growth brings forth significant challenges in the area of communication that needs to be addressed through innovative and creative engineering solutions.

The successful deployment of many applications enabled by next generation networks, such as high definition streaming, driver-less cars, and the Internet of Things (IoT), requires low latency real-time operation and high data rates. The peak data rate is expected to increase from hundreds of Mbps to tens of Gbps in the next few years [8]. One of the limiting factors that impedes the increase of data rates in current generation of wireless communication is the crowded spectrum at sub-6 GHz and thus the limited availability in the communication bands. To alleviate this issue, the next generation of wireless communication network will target higher frequencies, such as the millimeter-wave bands. This will enable the use of larger modulation bandwidths, thus lowering latency and increasing the date rate to the Gbps range. This is further demonstrated in Shannon-Hartley theorm, from which we know that the channel capacity, C, in bits per second, for a fixed signal to

noise ratio (SNR), scales linearly with an increase in the modulation bandwidth, B, and can be expressed as follows:

$$\text{C [bits/Sec]} = \text{B} \times \log_2(1 + \text{SNR}). \tag{1.1}$$

However, the migration to mm-wave radio frequencies (RF) brings about many challenges and an increase in design and hardware complexity. For instance, when dealing with higher modulation bandwidth signals, the nonidealities in the RF chain, such as the group delay and the non-flat frequency response of the chain, can significantly degrade the signal quality leading to an increase in the normalized mean square error (NMSE) between the received signal and the ideal signal as well as some deterioration in the error vector magnitude (EVM) at the signal symbol level. Ultimately, if not addressed, this leads to an increase in the bit error rate (BER) and a decrease in the peak achievable data rate. Moreover, the free-space path loss (FSPL), given by:

$$\text{FSPL [dB]} = 10\log_{10}\left(\left(\frac{4\pi R f}{c_0}\right)^2\right), \tag{1.2}$$

where c_0 is the speed of light in free space, scales quadratically with the increase in frequency, f. Hence, for a fixed transmitted power, P_{tx}, and fixed transmitter and receiver gain, G_{tx} and G_{rx} respectively, the received power, P_{rx}, can be expressed by Friis' equation as:

$$\text{P}_{\text{rx}}\ \text{[dBm]} = \text{G}_{\text{tx}}\ \text{[dBi]} + \text{P}_{\text{tx}}\ \text{[dBm]} + \text{G}_{\text{rx}}\ \text{[dBi]} - \text{FSPL [dB]}, \tag{1.3}$$

is greatly reduced at mm-wave frequencies compared to the sub-6 GHz bands. From 1.1, the effect of this would impact the channel capacity, due to the deterioration in SNR given a constant link distance, and would limit the coverage area of mm-wave base transceiver stations (BTS) when compared to their sub-6 GHz counterpart.

Furthermore, achieving high data rate communication links also requires the deployment of spectral efficient (in bit/s/Hz) and thus sophisticated modulation schemes, such as orthogonal frequency division multiplexing (OFDM) signals. Unfortunately, OFDM exhibits high peak-to-average-power-ratios (PAPRs) that greatly affect the signal amplification building blocks at the base station, i.e. power amplifiers (PAs), that are required to operate in backoff to avoid signal clipping or gain compression, and hence suffer from

severe degraded power efficiency. Alternatively, the PAs can be operated at higher efficient operating points, however, this calls for the deployment of linearization techniques such as digital predistortion (DPD) to mitigate the effect of the nonlinear behaviour and meet the adjacent channel power ratio (ACPR) and EVM requirements imposed by the federal communication community (FCC). For instance, DPD has been implemented in the previous generation of wireless communication systems to maximize the tradeoff between linearity and power efficiency and is expected to be an integral part in the next generation of communication systems especially given that mm-wave power amplifiers suffer from notably lower efficiency when compared to their sub-6 GHz counterpart.

While DPD schemes have been extensively studied in the literature, their successful deployment calls for several advancements to reduce their overall power over-head and complexity. Specifically, it is critical to reduce the requirements on the transmitter observation receiver (TOR) needed to train the DPD function. This includes decreasing the required sampling speed and bit resolution of the analog-to-digital converter (ADC) stage, the importance of which increases dramatically with the broadening of the bandwidth of the new generation of communication signals. In an attempt to tackle the challenges associated with DPD at mm-wave frequencies, this thesis proposes a novel single input single output (SISO) DPD scheme to linearize mm-wave hybrid-beamforming based large-scale multiple-antenna systems (LSMAS) using a feedback loop TOR with low bit resolution ADC and without affecting the DPD linearization capacity. For this, a novel DPD system architecture, that makes use of the inherent modularity of hybrid-beamforming arrays to minimize the hardware requirements of the TOR is first presented. The underlying challenges associated with its practical implementation, namely local oscillator (LO) phase-offset, delay alignment and channel calibration, are then addressed. Lastly, the validation and experimental results of the proposed DPD scheme on an off-the-shelf hybrid-beamforming array are presented.

Moreover, the complexity of the DPD engine for multiple-antenna arrays is also of primordial importance to address. For single PA systems, SISO DPD showed good linearization capacity. In order to extend the use of SISO DPD to LSMAS, the load modulation variation versus steering angles, due to the antenna coupling, needs to be investigated and addressed. In an attempt to tackle the challenges associated with the load modulation

for phased arrays, this thesis proposes, a generalized SISO DPD scheme trained at different steering angles, to minimize the variation in the EVM versus steering angles after DPD. This scheme is then compared to the SISO DPD trained at broadside and to the peace-wide DPD function in [5]. Afterward, an analysis of the variation in the array nonlinear behavior versus steering angels using the antennas S-parameters is proposed. Using this approach, the effect of tapering on the antennas reflected power is then investigated. Lastly, the validation and experimental results of a SISO DPD trained at broadside and of the proposed generalized SISO DPD on a commercial 64-elements array and with tapering applied are presented.

This thesis is organized into the following chapters. First, the background theory behind phased arrays, ADCs and DPD, as well as a literature review of the previous work on reducing the ADC power consumption and on DPD solutions for phased arrays are presented in Chapter 2. Chapter 3 then discusses the proposed reduced resolution DPD scheme and the experimental results. In chapter 4, a generalized SISO DPD is devised, an analysis of the load modulation on the array nonlinear behavior is presented and the effect of tapering on the impedance variance and on the DPD performance are presented. Lastly, the conclusions and the future work of this thesis are summarized in Chapter 5.

A note on the notational style: In thesis, RF signals are denoted without a subscript while Intermediate Frequencies (IF) signals are denoted with the subscript IF, i.e., $x(t)$ is an RF signal and $x_{IF}(t)$ is the corresponding IF signal. The complex baseband envelope of $x(t)$ is denoted in the text as $\tilde{x}(t)$. The discrete-time representation of $x(t)$, $x_{IF}(t)$ and $\tilde{x}(t)$ are $x[n]$, $x_{IF}[n]$ and $\tilde{x}[n]$, respectively. In addition, $\tilde{\mathbf{x}}(n)$ denotes a block of M samples, such that $\tilde{\mathbf{x}}(n) = \big(\tilde{x}[n], \tilde{x}[n-1], ..., \tilde{x}[n-M+1]\big)$. If $\tilde{x}[n]$ and $\tilde{h}[n]$ are two discrete time sequences, then $\big(\tilde{h} * \tilde{x}\big)[n] = \sum_k \tilde{h}[k]\tilde{x}[n-k]$ denotes the convolution of the sequence $\tilde{h}[n]$ with $\tilde{x}[n]$. Finally, $\big(\tilde{h} * \tilde{\mathbf{x}}\big)(n)$ denotes the vector $\big(\tilde{z}[n], \tilde{z}[n-1], ..., \tilde{z}[n-M+1]\big)$ where $\tilde{z}[n] = \big(\tilde{h} * \tilde{x}\big)[n]$

Chapter 2

Background Theory

2.1 Phased arrays for millimeter wave frequencies

Due to the increase in the free-space path loss at higher frequencies, phased arrays can be an attractive solution for mm-wave base stations. Increasing the number of transmitting antennas and combining their output at the user equipment (UE), has for effect to increase the array gain, G_{tx}, and thus the antenna isotropic radiated power (EIRP) defined as,

$$\text{EIRP [dBm]} = \text{G}_{\text{tx}} \text{ [dBi]} + \text{P}_{\text{tx}} \text{ [dBm]}, \tag{2.1}$$

and subsequently, from (1.3), increasing BTS coverage area given a constant targeted received power. It is to note that, the increase in the array gain is only achieved in the direction of maximum combining and can be further explained using the concept of array factor (AF). Fig. 2.1, shows an example of a linear array with N elements spaced by d, and where $\vec{r}_n$ designates the direction of propagation of the n^{th} antenna towards a receiver positioned at an angle θ and at a distance R in the far-field ($R \geq \frac{2D^2}{\lambda}$, where D is the antenna array length). Assuming that the antennas are excited using a signal tone source expressed in phasor form as, $\tilde{v}_n = |\tilde{v}_n|e^{j\phi_n}$, using (1.3), the far-field received power can then be expressed as follows:

$$\text{P}_{\text{rx}}(\text{R}, \theta) = \text{G}_{\text{a}} \text{ [dBi]} + \text{P}_{\text{tx}} \text{ [dBm]} + \text{G}_{\text{rx}} \text{ [dBi]} + \text{FSPL}(R) + 20\log_{10}\Big(\big|\text{AF}(\theta)\big|\Big), \tag{2.2}$$

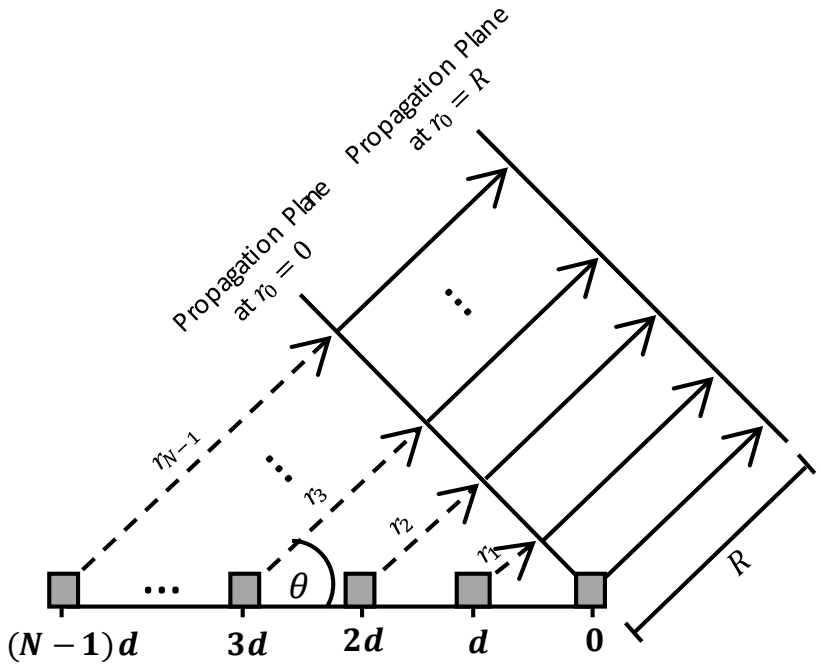

Figure 2.1: N Elements Linear Phased Array.

where

$$\begin{aligned} \left|\mathrm{AF}(\theta)\right| &= \left| \sum_{n=0}^{N-1} e^{j(\phi_n - \mathrm{kr_n} - \mathrm{kR})} \right| \\ &= \left| \sum_{n=0}^{N-1} e^{j(\phi_n - n\mathrm{k}d\cos\theta - \mathrm{kR})} \right| = \left| \sum_{n=0}^{N-1} e^{j(\phi_n - n\mathrm{k}d\cos\theta)} \right|, \end{aligned} \tag{2.3}$$

and G_a and $\mathrm{T_{tx}}$ are the gain and transmitted power per antenna respectively, $\mathrm{k} = \frac{2\pi}{\lambda}$ is the wave-number and ϕ_n are referred to as the beamforming coefficient of the n^{th} antenna

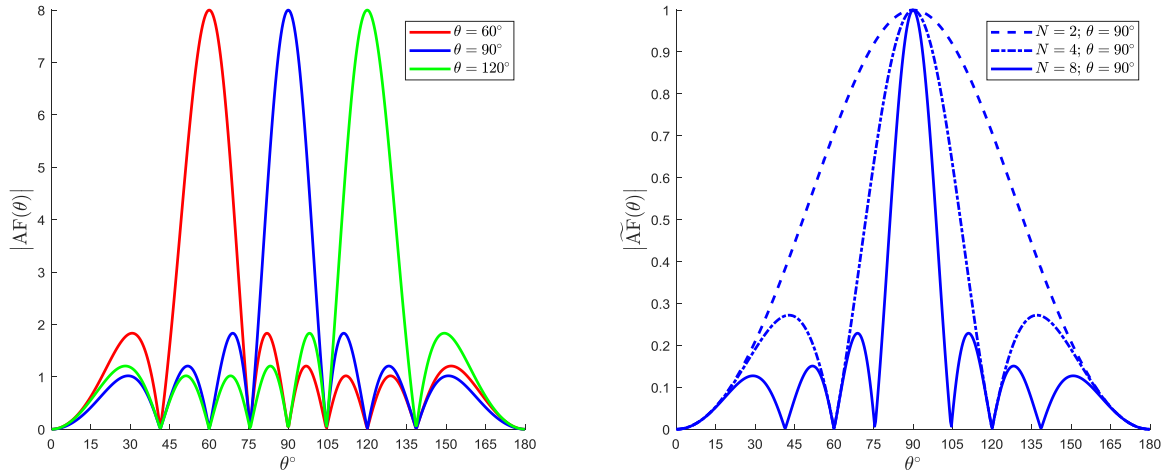

Figure 2.2: (Left) Array factor of a linear array versus θ; (Right) Normalized array factor versus N.

element. The normalized AF, denoted with a tilde, $\widetilde{\mathrm{AF}}$, can then be defined as follows:

$$\left|\widetilde{\mathrm{AF}}(\theta)\right| = \frac{1}{N}\left|\sum_{n=0}^{N-1} e^{j(\phi_n - n\mathrm{k}d\cos\theta)}\right|, \tag{2.4}$$

Subsequently, with proper element phasing, and in the direction of maximum combining, the transmitter array gain, $\mathrm{G_{tx}}$, scales linearly with the increase in number of elements and can be expressed as follows:

$$\begin{aligned} \mathrm{G_{tx}}\ [\mathrm{dBi}] &= \mathrm{G_a}\ [\mathrm{dBi}] + 20\log_{10}\big(|AF|\big) \\ &= \mathrm{G_a}\ [\mathrm{dBi}] + 20\log_{10}(N). \end{aligned} \tag{2.5}$$

The phased array technique can be further extended to a 2D array with antenna elements tiled with spacing d_x and d_y. In this configuration, the corresponding AF of an $N \times M$ array can be expressed as follows:

$$\mathrm{AF}(\theta,\phi) = \sum_{n=0}^{N-1}\sum_{m=0}^{M-1} e^{j(\phi_{n,m} - \mathrm{k}\sin\theta(nd_x\cos\phi - md_y\sin\phi))}, \tag{2.6}$$

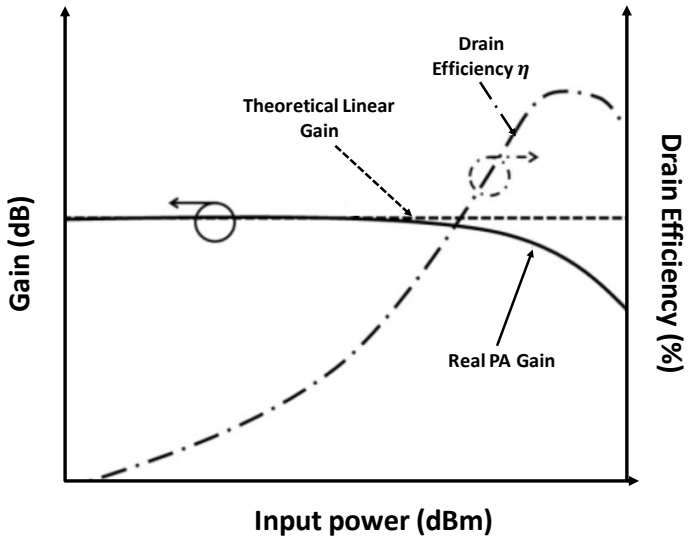

Figure 2.3: Linearity vs efficiency tradeoff.

where ϕ and θ designates the azimuthal and polar spherical coordinates of the far-field receiver.

2.2 Sidelobes reduction using tapering

The array factor pattern in Fig. 2.2 exhibits sidelobes that, if not addressed properly, can contribute to cause spacial interference with other users and hence affect the SNR and the achievable channel capacity.

A potential solution to reduce the sidelobes is via the use of windowing techniques inspired from the filter theory. This is relatively straight forward for the special case of linear arrays. Fig. 2.4, illustrates the use of different tapers, i.e. Chebyshev windowing and Taylor windowing, on a 64-elements 8×8 rectangular RF beamforming array. The sidelobes reduction achieved using tapering, however, comes at the cost of an increases in the half power beam width and a decrease in the array gain. Another application of

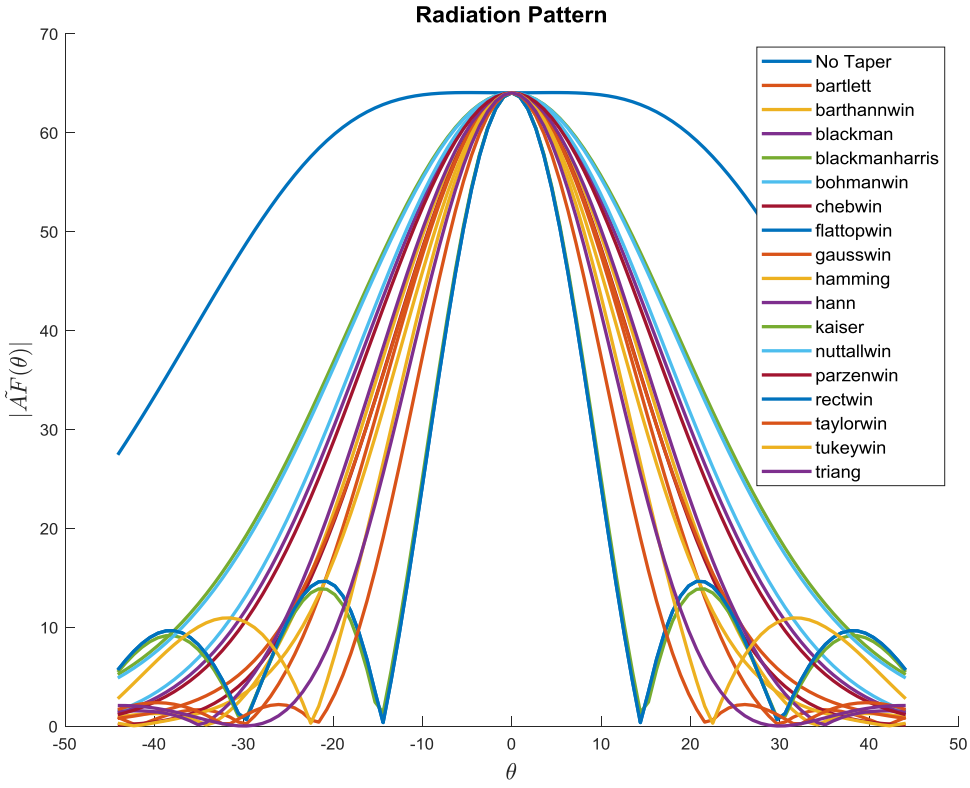

Figure 2.4: Radiation pattern of an 8×8 array using different tapers.

tapering for phased arrays is to generate wide beams for broadcasting applications. An example of such a taper is the flat-top window illustrated in Fig. 2.4.

In order to extend the application of tapering to 2-D arrays various techniques can be used. One of such approach is to obtain the 2-D window by rotating the frequency response of the 1-D window in the Fourier space and followed by the inverse Fourier transform [9]. Alternatively, the 2-D filter coefficients can be obtained by applying the McClellan transformation to the 1-D windows [10].

2.3 Power amplifier as an important nonlinear block

At the input of the BTS antennas, a PA stage is required to boost the signal power to an appropriate power level for signal transmission over the air and in order to meet the required coverage area. An ideal linear amplifier is assumed to have an input power independent gain, G, defined as:

$$G = \frac{P_{out}}{P_{in}}, \tag{2.7}$$

where P_{in} and P_{out} are the input and output power respectively. This is, however, very difficult to achieve for a wide range of input powers. In fact, for output powers higher that the P_{1dB}, defined as the output power point where the gain is 1dB lower than the linear gain, G, the PA becomes highly nonlinear. The nonlinear behaviour can be mitigated by operating the PA in the the back-off region where the gain is power independent. However, this will result in degraded drain and power added efficiency defined as:

$$\eta_{DE} = \frac{P_{out}}{P_{DC}}, \tag{2.8}$$

and

$$\eta_{PAE} = \frac{(P_{out} - P_{in})}{P_{in}}, \tag{2.9}$$

respectively, where P_{DC} is the Direct Current (DC) power consumption. Fig. 2.3, illustrates the tradeoff between efficiency and linearity, where the PA efficiency increases for higher input power.

2.3.1 PAPR

The PA is an amplitude sensitive device that exhibits power gain dependency near its peak output power. Spectral efficient signals have a time varying envelop, hence, if the PA is exhibiting a nonlinear behaviour, the instantaneous gain experienced by the input signal will vary with the input power. It is therefore important to define a metric that quantifies the variation of signal envelope power, and consequently, can be used to determine the power backoff level at which the PA can be driven before nonlinear distortions become

significant. To that end we define the PAPR of signal, $x(t)$, as:

$$\text{PAPR} = \frac{\max\big(|\tilde{x}(t)|^2\big)}{mean\big(|\tilde{x}(t)|^2\big)}. \tag{2.10}$$

For example, the input power needs to be backed-off by at least the PAPR from the PA maximum input power, P_{SAT}, in order to avoid saturating the amplifier.

The definition in (2.10) is, however, very stringent for most communication applications as it defines the PAPR based of the peak signal power while disregarding its occurrence rate. Alternatively, its more common to define the PAPR based of the complementary cumulative distribution function (CCDF) of the instantaneous power, $P(t)$, where:

$$P(t) = \frac{|\tilde{x}(t)|^2}{mean\big(|\tilde{x}(t)|^2\big)} \tag{2.11}$$

The CCDF defines the probability that $P(t)$ will be greater that a given value p_0. The PAPR is, hence, commonly defined as the p_0 which corresponds to the 0.1% CCDF point. Fig. 2.5, shows the CCDF of the instantaneous envelop power of spectrum efficient signals. It is clear from Fig. 2.5, that the PAPR increases for higher-order modulation techniques and is the highest for OFDM signals. Consequently, spectrum efficient signals, such as OFDM signals, would require the PA to operate in high backoff and with low efficiency in order to avoid nonlinear behaviour. Alternatively, it is possible to use DPD techniques to characterize and compensate for the PA nonlinearity and hence, achieving high efficiency operation.

2.3.2 Gain Distortion and AM/PM

In order to compensate for the PA nonlinear distortion, we first need to accurately measure and characterize the PA nonlinearity. The Gain Distortion and AM/PM are visual tools that can be used to quantify the PA power dependent behaviour. In the Gain Distortion curve, the instantaneous PA power gain, $\frac{P_y[n]}{P_x[n]}$, is plotted versus the instantaneous PA input power, $P_x[n]$. For PAs that exhibit nonlinear behavior, the Gain Distortion curve shows a gain drop as the input power increases. Similarly, in the AM/PM, the phase response

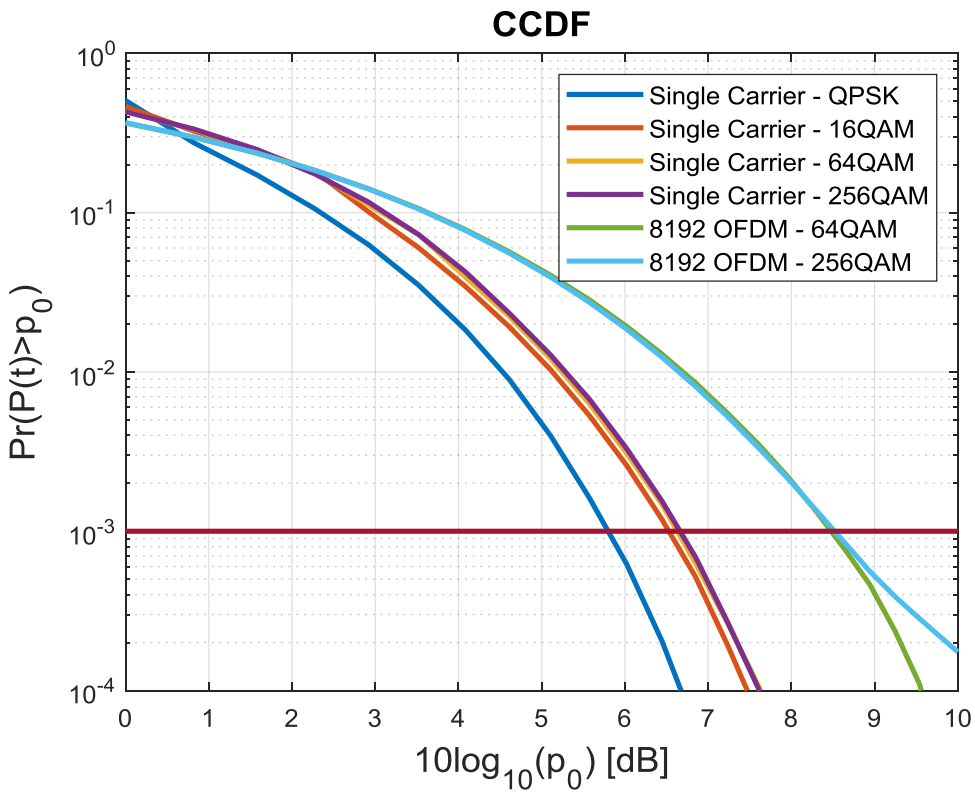

Figure 2.5: CCDF of the instantaneous envelop power, $P(t)$, for different spectral efficient signals.

of the instantaneous power gain, is plotted versus the instantaneous input power. The AM/PM illustrates the power dependent phase attributed distortion created by the PA. An example of the gain and phase distortion curves of a nonlinear PA driven by modulated signals is shown in Fig. 2.6.

2.3.3 Memoryless versus dynamic systems

The PA nonlinear behavior can often be classified as static or dynamic distortion. A memoryless (static) PA nonlinear behavior produces distortions that do not depend on the

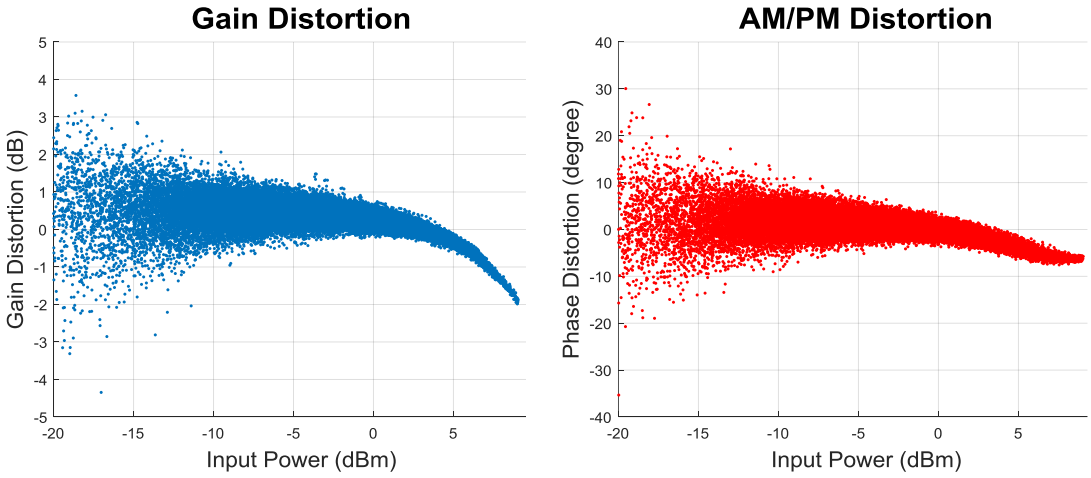

Figure 2.6: Gain Distortion and AM/PM of an nonideal PA.

input signal past values and, hence, can be modeled using a simple polynomial:

$$y(t) = \alpha_0 + \alpha_1 x(t) + \alpha_2 x^2(t) + \alpha_3 x^3(t) + ..., \tag{2.12}$$

where $x(t)$ and $y(t)$ are the PA input and output signals respectively. On the other hand, a dynamic nonlinear behavior generates distortions that depend on the input signal past values. Such distortion can be modeled using an augmented Weiner or augmented Hammerstein model, [11, 12].

2.4 Digital predistortion DPD

PAs are most efficient near their saturation power level where they exhibit nonlinear behaviour. Advanced PA power efficiency enhancement techniques have been investigated in the literature. These include Doherty PAs, outphasing techniques, and envelop tracking. Yet, the successful deployment of PAs calls for the use of linearization techniques, such as digital predistotion, to mitigate the distortions exhibited by the high efficiency PAs.

2.4.1 Forward modeling

The PA nonlinear behavior can be described using the complex baseband Volterra equivalent (CBBE) series [13], such that the PA equivalent baseband signal, $\tilde{y}[n]$, is expressed as linear combination of the discrete baseband input signal, $\tilde{x}[n]$, as follows:

$$\tilde{y}[n] = \sum_{k=0}^{N} \sum_{\mathbf{m}_1 \in L^k} \sum_{\mathbf{m}_2 \in L^{k+1}} \tilde{f}^k_{\mathbf{m}_1,\mathbf{m}_2} \prod_{i=1}^{k} \tilde{x}^*[n - \mathbf{m}_1(i)] \prod_{j=1}^{k+1} \tilde{x}[n - \mathbf{m}_2(j)], \tag{2.13}$$

where $2N+1$ is the highest static nonlinearity order, $\tilde{f}^k_{\mathbf{m}_1,\mathbf{m}_2}$ are the Volterra kernels, M is the memory depth and L^k are the sets defined as

$$L^k = \big\{\mathbf{m} \in \{0, ..., M-1\}^k, |0 \leq \mathbf{m}(1) \leq ... \leq \mathbf{m}(k) \leq M-1\big\} \tag{2.14}$$

If the PA exhibit memoryless static nonlinearity, then all the memory lags are 0, i.e. $\tilde{f}^k_{\mathbf{m}_1,\mathbf{m}_2} = 0$ when $\mathbf{m}_1 > 0$ or $\mathbf{m}_2 > 0$, and the CBBE can be expressed as follows:

$$\tilde{y}[n] = \sum_{k=0}^{2N} \tilde{x}[n]\big|\tilde{x}[n]\big|^k. \tag{2.15}$$

Due to the complexity and large number for kernels used by the CBBE model, various attempts have been made to reduce the Volterra series complexity, including the pruned Volterra model presented in [17], the General Memory Polynomial model (GMP) proposed in [18], and the dynamic deviation reduction (DDR) introduced in [19]. In this thesis, the Complexity-Reduced Volterra model (CRV), first outlined in [20], is used to model the PA and is expressed as follows:

$$\tilde{y}[n] = \sum_{l=0}^{L} a_l \tilde{\psi}_l\big(\tilde{\mathbf{x}}[n]\big), \tag{2.16}$$

where the basis functions, $\tilde{\psi}_l\big(\tilde{\mathbf{x}}[n]\big)$ are chosen to be

$$\tilde{\psi}_l\big(\tilde{\mathbf{x}}[n]\big) = \tilde{x}[n - m_l^{'}]\big|\tilde{x}[n - m_l]\big|^{2p_l}, \tag{2.17}$$

such that the l^{th} polynomial basis function, $\tilde{\psi}_l(.)$, is of order $2p_l + 1$ with lags $m_l^{'}$ and m_l.

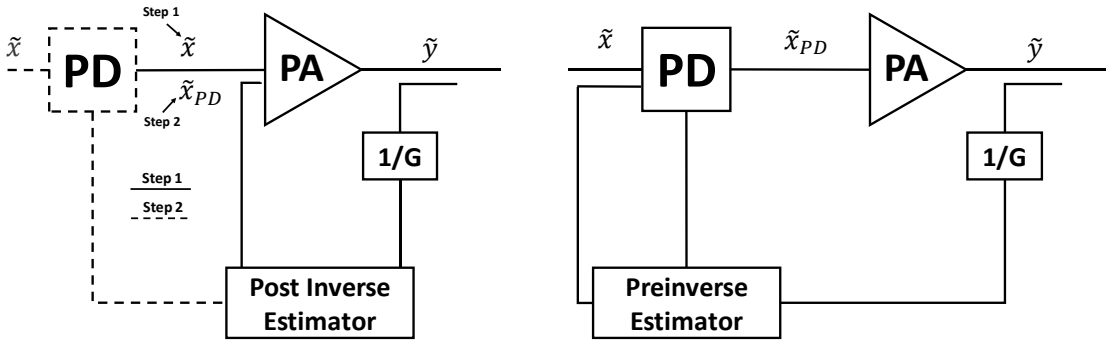

Figure 2.7: Learning architecture to train the predistoter modules: (Left) Indirect learning; (Right) Direct learning.

In order to identify the PA model coefficients, the input and output baseband signals relationship described in (2.16) can be rewritten in matrix form:

$$\tilde{\mathbf{y}} = \tilde{\Psi}\mathbf{a} + \tilde{\boldsymbol{\epsilon}}, \tag{2.18}$$

where $\mathbf{a} = (a_1, ..., a_L)$ are the model coefficients, $\tilde{\boldsymbol{\epsilon}}$ is modeling error and $\tilde{\Psi}$ is the basis matrix with entries in the i^{th} row and j^{th} column given by

$$\left[\tilde{\Psi}(\tilde{\mathbf{x}})\right]_{i,j} = \psi_j\big(\tilde{\mathbf{x}}[n+i-1]\big). \tag{2.19}$$

The parameters $\mathbf{a}$ are then given from (2.18) by minimizing the squared l_2 norm of the modeling error, i.e. minimizing

$$\begin{aligned} J =& \| \tilde{\boldsymbol{\epsilon}} \|_2^2 \\ =& \| \tilde{\mathbf{y}} - \tilde{\Psi}\mathbf{a} \|_2^2 \\ =& \sum_n \left| \tilde{y}[n] - \sum_{l=0}^{L} a_l \tilde{\psi}_l\big(\tilde{\mathbf{x}}[n]\big) \right|^2. \end{aligned} \tag{2.20}$$

This is a standard least-square fit, with the well known solution:

$$\mathbf{a} = \big(\Psi(\tilde{\mathbf{x}})^H \Psi(\tilde{\mathbf{x}})\big)^{-1} \Psi(\tilde{\mathbf{x}})^H \tilde{\mathbf{y}}. \tag{2.21}$$

Alternatively, the parameters can be estimated using more computational efficient algorithm such as recursive least square (RLS) for optimal hardware implementation.

2.4.2 Direct and indirect learning

In the DPD formulation, the predistorter (PD) model is modeled using similar basis functions as the forward model, i.e., Volterra series or CRV, and can be expressed as follows:

$$\tilde{x}_{PD}[n] = \sum_{l=0}^{L_{PD}} c_l \tilde{\psi}_l\big(\tilde{\mathbf{x}}[n]\big), \tag{2.22}$$

where $\tilde{x}_{PD}[n]$ is the predistorted signal, L_{PD} is the total number of basis of the linearizer and c_l are the DPD coefficients. In order to identify the PD parameters, two approaches are commonly used in the literature. The indirect learning approach, illustrated in Fig. 2.7 (Left), assumes that the PA pre-inverse and post-inverse are identical such that:

$$\tilde{f}_{PA}^{-1}\big(\tilde{y}[n]\big) = \tilde{x} \Rightarrow \tilde{x}_{PD}[n] = \tilde{f}_{PA}^{-1}\big(\tilde{x}[n]\big) \tag{2.23}$$

where $\tilde{f}_{PA}^{-1}$ is the PA post inverse model functions. As a results, the PD's coefficients, $\mathbf{c}$ are estimated using the post inverse's least square solution given by

$$\mathbf{c} = \big(\Psi^H(\tilde{\mathbf{y}})\Psi(\tilde{\mathbf{y}})\big)^{-1}\Psi(\tilde{\mathbf{y}}^H)\tilde{\mathbf{x}}. \tag{2.24}$$

In the direct learning case, illustrated in Fig. 2.7 (Right), the PD parameters are identified iteratively by minimizing the LSE, $\tilde{e}[n] = \tilde{y}[n] - \tilde{x}[n]$, between the PA output signal $\tilde{y}[n]$ and the desired signal $\tilde{x}[n]$. For this, blocks of the baseband input $\tilde{x}[n]$ and corresponding error $\tilde{e}[n] = \tilde{y}[n] - \tilde{x}[n]$ are used to iteratively refine the estimate of $\mathbf{c}$. Using this approach, the nonlinear distortion of the PA is modeled as an additive error and can be written as:

$$\tilde{f}_{PA}\big(\tilde{\mathbf{x}}\big) = \tilde{x}[n] + \tilde{e}\big(\tilde{\mathbf{x}}\big) \tag{2.25}$$

2.4.3 Single PA DPD model using direct learning

To apply the DPD model given by (2.19) and (2.22) using the direct learning approach, first the underlying coefficients $\mathbf{c} = (c_1, ..., c_{L_{PD}}) \in \mathbb{C}^{L_{PD}}$ must be identified. This yields a sequence $\mathbf{c}^{(1)}$, $\mathbf{c}^{(2)}$,..., $\mathbf{c}^{(N)}$ of N estimates of the the pre-distorter coefficients. Specifically, before the 1st iteration, the pre-distorter is chosen to pass $\tilde{x}[n]$ undistorted, i.e.,

$$\mathbf{c}^1 = (1, 0, ..., 0), \tag{2.26}$$

and the coefficients after the k^{th} iteration, $1 \leq k \leq N-1$, are updated according to

$$\mathbf{c}^{k+1} = \mathbf{c}^k - \gamma \Delta \mathbf{c}^k \tag{2.27}$$

where $0 < \gamma < 1$ is the update step size, and $\Delta \mathbf{c}^{(k)} \in \mathbb{C}^{L_{PD}}$ is the update direction of the predistorter model coefficients. To determine the update direction $\Delta \mathbf{c}^{(k)}$ of the predistortion model coefficients, for the k^{th} iteration, we fit the error $\tilde{e}[n_k]$ over a block of N samples as

$$\tilde{\mathbf{e}}^{(k)} = \Psi^{(k)} \Delta \mathbf{c}^{(k)} + \tilde{\boldsymbol{\epsilon}}^{(k)} \tag{2.28}$$

where

$$\tilde{\mathbf{e}}^{(k)} = \big(\tilde{e}[n_k], ..., \tilde{e}[n_k + N - 1]\big)^T, \tag{2.29}$$

is the block of N error samples at the k^{th} iteration, $\tilde{\boldsymbol{\epsilon}}^{(k)} = \big(\tilde{\epsilon}[n_k], ..., \tilde{\epsilon}[n_k + N - 1]\big)^T$ is the modelling error in fitting $\Delta \mathbf{c}^{(k)}$, and $\Psi^{(k)}$ is a $N \times L$ matrix with entry in the i^{th} row and j^{th} column given by

$$\Big[\Psi^{(k)}\Big]_{i,j} = \psi_j(\tilde{x}[n_k + i - 1]). \tag{2.30}$$

Given $\tilde{x}[n]$ and $\tilde{e}[n]$ for $n = n_k, ..., n_k + N - 1$, to determine the update direction $\Delta \mathbf{c}^{(k)}$ from (2.28) that minimize the squared l_2 norm of the modeling error, i.e., that minimize

$$\begin{aligned} J =& \| \tilde{\boldsymbol{\epsilon}}^{(k)} \|_2^2 \\ =& \| \tilde{\mathbf{e}}^{(k)} - \Psi^{(k)} \Delta \mathbf{c}^{(k)} \|_2^2 \\ =& \sum_{n=n_k}^{n_k+N-1} \left| \tilde{e}^{(k)}[n] - \sum_{l=1}^{L} c_l^{(k)} \psi_l\big(\tilde{\mathbf{x}}[n]\big) \right|^2. \end{aligned} \tag{2.31}$$

are determined with standard least-square fit, with well known solution

$$\Delta \mathbf{c}^{(k)} = \big(\Psi(\tilde{\mathbf{x}})^H \Psi(\tilde{\mathbf{x}})\big)^{-1} \Psi(\tilde{\mathbf{x}})^H \tilde{\mathbf{e}}^{(k)}. \tag{2.32}$$

Hence, (2.27), (2.28), (2.30) and (2.32) comprise the iterative training process to identify the predistortion coefficients.

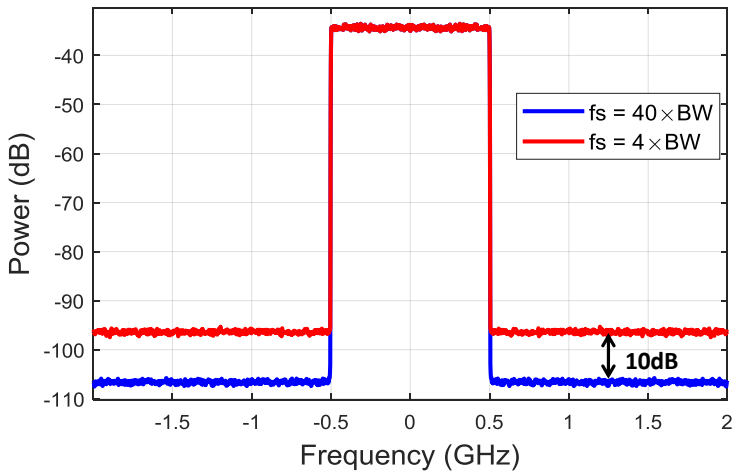

Figure 2.8: 1 GHz OFDM signal sampled using $fs = 4 \times BW$ and $fs = 40 \times BW$.

2.5 Overview of analog to digital converters theory

In order to sample the PA output signal required for the DPD training, a signal acquisition block is required to digitize the analog signal. The ADC is a signal acquisition block that samples the input waveform and generates a finite binary representation of the voltage levels. This process, however, introduces quantization error denoted by e_q and imposes a limit on the digitized signal SNR that can observed.

2.5.1 Oversampling

The SNR of an ideal ADC under an input sine wave excitation, v_{in}, can be expressed as a function of the ADC resolution, N, as follows:

$$\begin{aligned} \text{SNR [dB]} &= 10\text{log10}\left(\frac{\overline{v_{in}^2}}{\overline{e_q^2}}\right) \\ &= 6.02\text{N} + 1.76. \end{aligned} \tag{2.33}$$

In many applications, however, the the captured signal observed bandwidth, is less than ADC bandwidth defined as $\frac{f_s}{2}$ where f_s is the ADC sampling rate. It is possible then to use digital processing to filter out the excess noise outside the wanted observation bandwidth, BW, and improve the SNR. Using this concept, (2.33) can be rewritten as:

$$\text{SNR(dB)} = 6.02\text{N} + 1.76 + 10\log10\left(\frac{f_s}{2 \cdot BW}\right). \tag{2.34}$$

This technique is commonly referred to as oversampling. Fig. 2.8, shows an example of a signal with oversampling factor of 4 and with an oversampling factor of 40. From Fig. 2.8, it can be clear seen that the signal quantized using an oversampling ratio of 40 has around 10 dB of SNR improvement when compared to the signal sampled using an oversampling ratio of 4. This increase in the SNR is equivalent to an increase in the ADC bit resolution in (2.33). Consequently, using (2.34), it is possible to define an effective number of bits (ENOB) that reflects the effective resolution gain due to the oversampling factor and can be expressed as follows:

$$\text{ENOB(bits)} = \frac{\text{SNR} - 1.76}{6.02}. \tag{2.35}$$

2.5.2 ADC figure of merit

Reducing the ADC power consumption is detrimental for the successful deployment of mm-wave digital predistortion techniques and hence it is important to define a framework that can be used to assess and compare the ADCs power consumption irrespective of their architecture. Such framework that IEEE has relied on is the Figure Of Merit (FOM) calculation described below:

$$\text{FOM} = \frac{\text{Power}}{2^{\text{ENOB}} \times f_s}. \tag{2.36}$$

From (2.36), it can be observed that the ADC power consumption scales linearly with an increase in the sampling rate and quadratically with an increase in bit resolution.

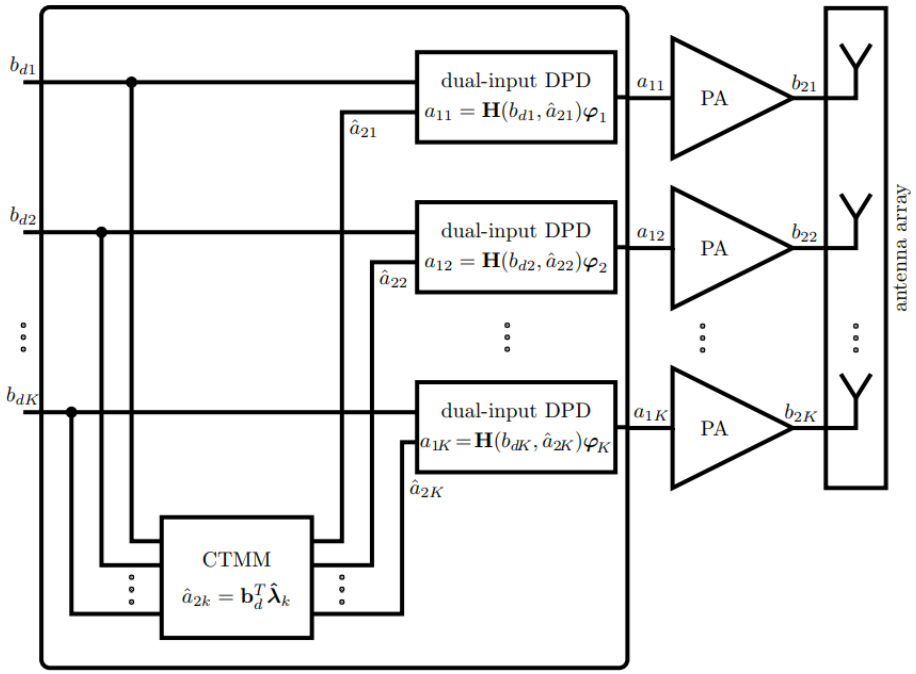

Figure 2.9: Dual-input DPD scheme using antenna coupling matrix to estimate the reverse waves [1]

2.6 Literature on DPD for antenna arrays

There have been some attempts to extend the application of DPD to multiple-antenna transmitter arrays at mm-wave frequencies. These can be classified into two distinct categories: those that use multi-input (mainly dual-input) modelling approaches (i.e., with both the forward and reverse waves provided as inputs to the model), and those based on single-input single-output (SISO) modelling approaches (i.e., with only forward waves provided as inputs). Both types of approaches have shown an aptitude to linearize 5G Large Scale Massive Antenna Systems (LSMAS).

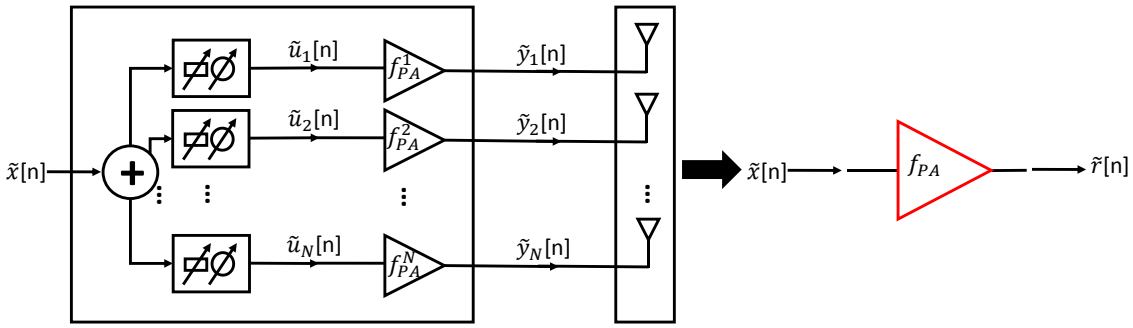

Figure 2.10: Single-input SISO DPD model for RF beamforming arrays.

2.6.1 Dual-input DPD scheme

The dual-input DPD scheme proposed in [14, 1] is trained using the individual PAs forward and reverse wave, and then used in conjunction with a cross-talk and mismatch model to linearize a 4-element digital beamforming array operating at 2.12 GHz and driven with 5 MHz modulated signals. Fig. 2.9 illustrate a system block diagram of the proposed DPD scheme, where the forward waves are sampled at the PA outputs using directional couplers and the reverse waves are generated using the antennas coupling matrix. In [14, 1], the PAs S_{22}'s are assumed to be very low and hence ignored while estimating the reverse waves. The PA output signal b_{2k} of the k^{th} static PA can then be modeled as a function of the input signal a_{1k} and the reverse wave a_{2k} as follows:

$$b_{2k} = \sum_{p=0}^{(P-1/2-1)} \sum_{v=0}^{p} \sum_{u=0}^{p+1} \alpha_{kpvu} {a_{1k}}^{p+1} {a_{1k}^*}^{p-v} {a_{2k}}^{u} {a_{2k}^*}^{v} \tag{2.37}$$

where α_{kpvu} are the model complex coefficients and P is the static nonlinearity order. This formulation is similar to the dual-band DPD formuation. A similar dual-input DPD scheme was also used in [15, 16] to predict the behavior of beamforming arrays formed of simulated PA models. In this approach the forward and reverse waves are assumed to be known. A practical implementation of the feedback path in [15, 16], would be using couplers at the PA outputs to measure the forward and reverse waves.

2.6.2 Single-input DPD scheme

In terms of single-input approaches, lower complexity SISO DPD solutions have also demonstrated interesting linearization capacity when applied to LSMAS driven with 5G signals. For example, in [17, 18], a SISO model is applied in simulation to linearize both a hybrid and an RF beamforming array. Using this approach the array system is modeled as a single PA system, illustrated in Fig. 2.10, and is trained using the sum of the PA outputs. In [19, 20, 5], the capacity of a SISO model to linearize a sub-6 GHz 2x2 array driven by 10 MHz modulated signals, a 16-element array at 2 GHz driven with 20 MHz modulated signals, and a mm-wave 64-element RF beam-forming array driven with up to 800 MHz signals, was experimentally validated. The feedback signals in [19] are sampled using couplers at the PA outputs and digitally summed to form the DPD training signal. Alternatively, the authors in [20], trained the DPD signal using an anti-beamforming transmitter observation receiver (TOR) module that generates a far-field equivalent signal. Finally, in [18, 5], a far-field probing antenna was used to generate the feedback signal needed for DPD.

2.6.3 Limitation of the existing schemes

While the reported works have been successful in demonstrating the applicability of DPD for arrays, challenges to its practical implementation on commercial products are yet to be addressed. For instance, the dual input DPD model introduced in [14, 1] requires couplers at the PA outputs to sample the forward and reverse waves required for DPD training or a prior knowledge of the cross-coupling matrix. This approach is, however, impractical for mm-wave arrays, due to the large number of PA elements and the compact size of the array. Alternatively, SISO models trained using over the air combining in [18, 5] can offer a more attractive solution as it does not require additional design overhead on the array system. This approach however, is limited by the nonidealities in the array such as the load modulation, and requires a peace-wise beam steering angle dependent sets of DPD coefficients to linearize the array for different combination of θ and ϕ. Moreover, despite the issues relating the practical implementation of the DPD feedback path, the successful

deployment of DPD also calls for several advancements to reduce the TOR overall power overhead and complexity.

2.7 Literature review on reduced complexity TOR for DPDs

There have been multiple attempts in the literature on reducing the DPD TOR overall complexity and power consumption. This includes decreasing the required sampling speed and bit resolution of the analog-to-digital converter stage. The importance of the latter increases dramatically with the broadening of the signal bandwidth at mm-wave frequencies. These attempts can be categorized into two main groups, i) Subsampling DPD and ii) reduced resolution DPD.

2.7.1 Subsampling DPD

This approach is commonly used in the literature to reduce the TOR power consumption by reducing the the ADC sampling speed from $10\times$ the signal bandwidth to $F\times$ the signal bandwidth where $0 < F < 10$.

Band-limited DPD

In [2, 21, 22], a band limited DPD scheme was proposed to lower the TOR's ADC sampling rate while avoiding aliasing by limiting the bandwidth of the PA's output signal using a bandpass filter. Fig. 2.11 provide a system block diagram of the proposed scheme. Using this approach, the DPD basis functions in (2.22) needed to be adjusted to accommodate for the band limiting function $H(.)$ and can be expressed as follows:

$$\tilde{x}_{PD}[n] = \sum_{l=0}^{L_{PD}} c_l H\Big(\tilde{\psi}_l\big(\tilde{\mathbf{x}}[n]\big)\Big), \tag{2.38}$$

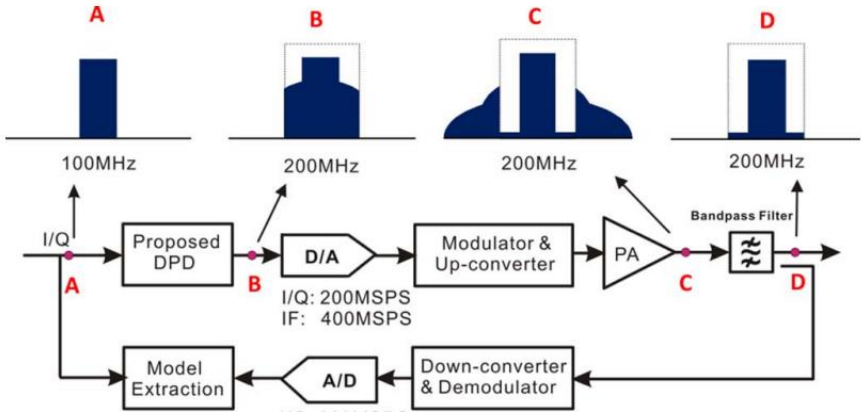

Figure 2.11: Band-limited DPD [2].

By applying this approach, the authors could linearize the PA output signal within the bandpass filter bandwidth and is further illustrated in Fig. 2.12 where a comparison between the proposed scheme using a sampling rate $f_s = 2 \times 40\text{MHz}$ and conventional DPD using $f_s = 2 \times 140\text{MHz}$ is provided. Hence, by reducing the required feedback signal bandwidth and including a band limiting function in the DPD formulation, the ADC sampling rate can be reduced. The drawback of this technique is that it required the use of additional bandpass filters at the PA output hence making it impractical for an array of PAs. This approach is also limited to weak nonlinear memory systems.

Subsampling restoration

Alternatively, the authors in [3] proposed a sampling rate relaxation technique that uses low ADC sampling speed along with increased capture time and signal processing in order to reconstruct the original signal without information loss. For the simple case of reducing the required sampling rate f_s by a factor of 2, the original signal waveform is sampled at the initial sampling rate f_s and a second copy of the desired signal is appended to the first copy after applying a one-sample delay. Accordingly, sampling the received signal at a sampling rate of $\frac{f_s}{2}$ will result in the acquisition of the odd indexed desired samples in the first half of the received signal and the even indexed desired terms in the second half of the received

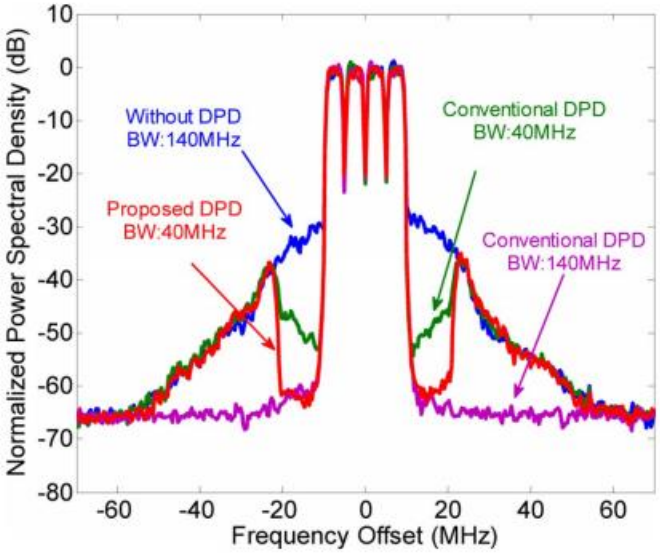

Figure 2.12: Band-limited DPD spectrum results [2].

signal. Thus, by rearranging the samples, the desired full rate signal sampled at f_s can be recomposed. This process is further demonstrated in Fig. 2.13, where the received samples (Left) and the digitally reconstructed desired signal (Right) are illustrated. The main disadvantage of this method is that the discontinuity introduced in the transmitted signal can cause some spectral regrowth and can alter the PA input signal characteristics, hence limiting the DPD linearization capability. Moreover, this method requires an increase in the acquisition time and therefore the reduction of the power consumption due to the use of lower sampling speed is reduced.

2.7.2 Reduced resolution DPD

While the investigation to reduce the TOR sampling speed showed potential, attempts to reduce the required ADC bit resolution has not seen further significant research attention. In fact, only recently was a new DPD system proposed in [4] that investigated the utilization of 1-bit complex ADC receiver for DPD training. A block diagram of the proposed system

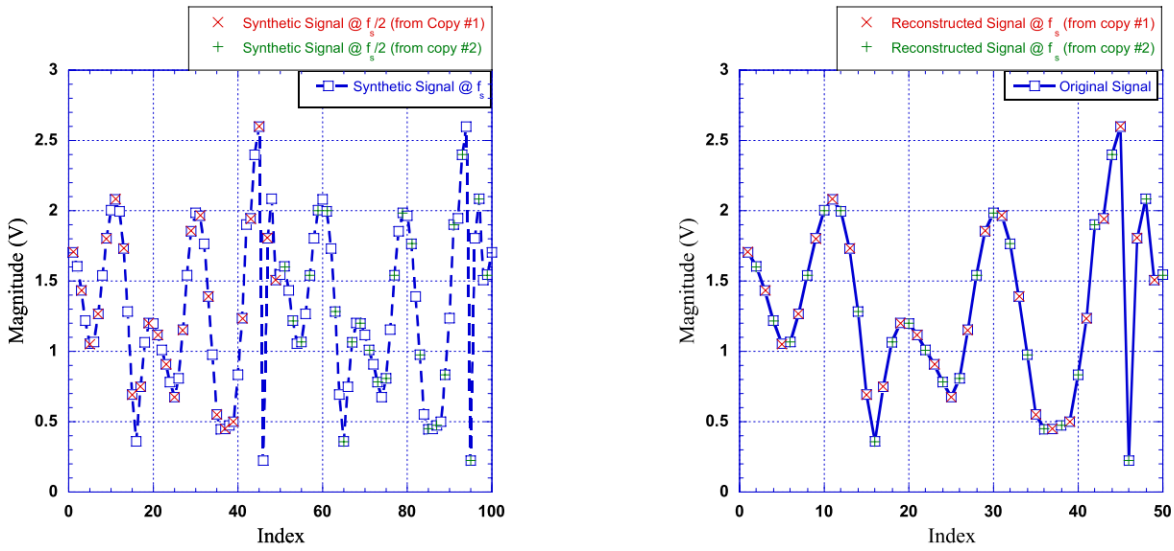

Figure 2.13: Subsampling restoration [3]: (Left) Received sampled signal (Right) Restored signal.

is shown in Fig. 2.14. The least square estimate of the DPD coefficients can then be rewritten as follows:

$$\Delta_{\mathbf{c}}^{(k)} = \gamma^{(k)}\big(\Psi(\tilde{\mathbf{x}})^H\Psi(\tilde{\mathbf{x}})\big)^{-1}\Psi(\tilde{\mathbf{x}})^H{\Delta_{\mathbf{s}}}^{(k)}, \tag{2.39}$$

where $\gamma^{(k)}$ is the k^{th} iteration learning parameter and $\Delta_{\mathbf{s}}^{(k)}$ is the k^{th} iteration error signal captured using the 1-bit complex ADC and can be further described as

$$\Delta_s^{(k)} = sign(\tilde{y}_I^{(k)}[n] - \tilde{x}_I[n]) + jsign(\tilde{y}_Q^{(k)}[n] - \tilde{x}_Q[n]). \tag{2.40}$$

This approach is, however, highly dependent on the learning parameter $\gamma^{(k)}$ which is critical to the linearization performance as well as to the convergence speed. This method, also, requires the deployment of two additional high speed digital to analog converters to generate an ideal copy of the desired signal needed at the comparators input stage, a pre-characterization of the Device Under Test (DUT) AM/AM curve to estimate the learning parameters required for the DPD training and a large number of iterations to reach convergence of the training algorithm. Time alignment between the ideal signal generated by the additional DACs and the PA baseband output is also critical in achieving

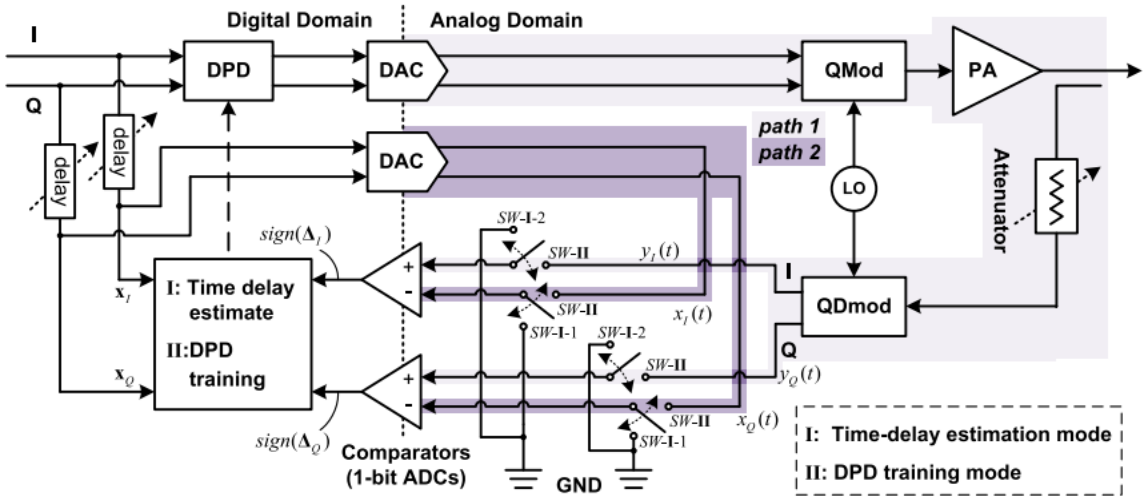

Figure 2.14: Reduced resolution DPD using 1-bit complex ADC [4].

optimal results. This is however difficult to achieve given the 1-bit complex receiver. Consequently, the power consumption reduction achieved thanks to the reduced receiver ADC resolution comes at the cost of significant added complexity and hence limits the practical implementation of this scheme.

2.7.3 Conclusion

In this chapter, phased arrays and data acquisition blocks were reviewed. Problems with PAs at high frequencies and their effects on the ACPR and EVM were discussed. To mitigate the effect of the PA nonlinearity, DPD solution for single PA and phased arrays were devised. Although DPD is widely adopted for sub-6 GHz systems, the challenges of its practical implementation at mm-waves were presented. More specifically, in order to accommodate for the load modulation exhibited by phased arrays, multiple solutions in the literature were proposed ranging from dual-input DPD that sample the forward and reverse waves to single input peace-wise SISO DPD techniques. However, the proposed solutions require added hardware and signal processing overhead that limits their real life

deployment. A literate review of exiting TOR power consumption reduction techniques were also introduced. Out of this review it was evident that practical implementation of Subsampling and reduced resolution DPD were missing, the importance of which increases dramatically, as the signal bandwidth increases. For that reason, a new DPD scheme is proposed to linearize mm-wave hybrid-beamforming based LSMAS while using a TOR with low bit resolution ADC and without added hardware or signal processing complexity. A study of the effect of tapering on the load modulation is also presented and results demonstrating the use of a single set of coefficients to linearize a commercial array at different beam-steering angles are shown.

Chapter 3

Reduced Resolution Transmitter Observation Receiver Digital Pre-Distorion Scheme

In this chapter, the proposed reduced resolution TOR receiver DPD scheme and its theoretical basis are presented. Afterward, the underlying challenges associated with its practical implementation, namely local oscillator (LO) phase-offset and delay alignment and describes methods devised to tackle these challenges. Finally experimental results are presented and conclusions of the work are summarized. The work in this chapter is based on the work in **??**

3.1 Proposed DPD Scheme using Reduced Resolution TOR and Theoretical Formulation

Fig. 3.1 shows the high-level block diagram of the proposed SISO DPD scheme applied to a hybrid beamforming system with, for simplicity of exposition, two sub-arrays. The proposed scheme exploits the inherent modularity of the hybrid-beamforming system to minimize the hardware requirements of the TOR. It takes advantage of the fact that the

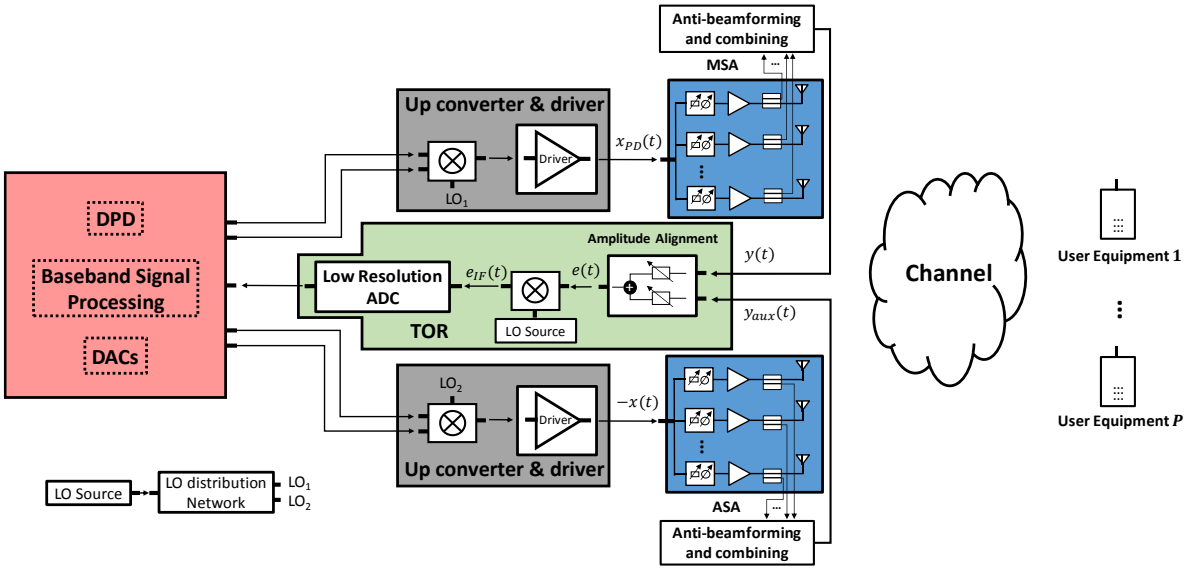

Figure 3.1: Block diagram of proposed DPD system for the case of a two sub-array hybrid beamformer: main sub-array transmits $x_{PD}(t)$; auxiliary sub-array transmits $-x(t)$.

training of the DPD function for each sub-array is conducted separately using a weighted sum of the constituent sub-array outputs. We denote the sub-array to be linearized as the main sub-array (MSA); the second sub-array is referred to as the auxiliary sub-array (ASA). During the DPD training process, the MSA transmits a pre-distorted input $x_{PD}(t)$of the desired RF signal $x(t)$, while the ASA is mobilized to transmit an inverted instance $-x(t)$ of the desired signal $x(t)$. In the following, the anti-beamforming module connected to the MSA allows for the generation of a weighted sum, $y(t)$, of the signals transmitted by the constituent MSA antennas. This is used to emulate the signal that would be received by a far-field antenna and includes distortions attributed to the PAs in the MSA. Similarly, the anti-beamforming module connected to the ASA generates an output signal denoted by $y_{aux}(t)$. It is of note that as the ASA operates in backoff during the training phase, the corresponding signal at the anti-beamforming module,$y_{aux}(t)$, will be a replica of the inverse $-x(t)$. To ensure proper cancellation of $x(t)$ in $y(t)$, and to generate the error (distortion) signal $e(t)$ that will be used for DPD training, two attenuators are used to adjust the magnitudes of $y(t)$ and $y_{aux}(t)$. To simplify the theoretical derivations of the

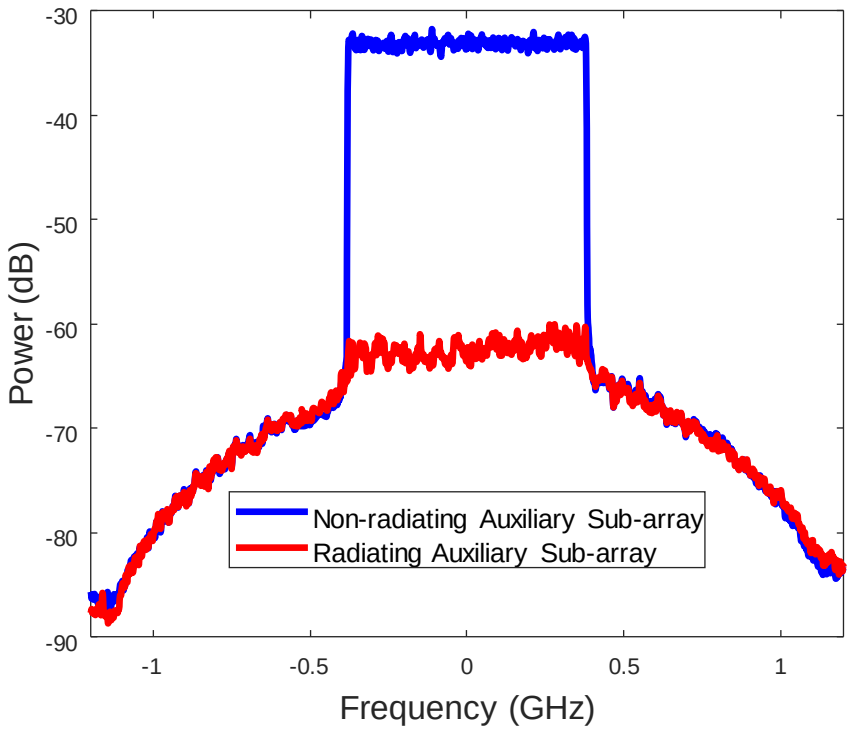

Figure 3.2: Power spectrum density of the MSA transmitted signal and corresponding error signal $e(t)$.

proposed DPD scheme, the following expression of the error signal is written as assuming proper amplitude alignment of $y(t)$ and $y_{aux}(t)$:

$$\begin{aligned} e(t) &= y(t) + y_{aux}(t) \\ &= y(t) - x(t) \end{aligned} \tag{3.1}$$

The error signal is then down-converted to IF to obtain $e_{IF}(t)$, digitized using an ADC to obtain $e_{IF}[n]$, and further digitally down-converted to obtain the complex baseband signal $\tilde{e}[n]$. Fig. 3.2 shows an example of the MSA transmitted signal, $y(t)$, and the corresponding error signal, $e(t)$. In this case the input signal $x(t)$ is an 800 MHz OFDM signal and the MSA and ASA are instances of a 64-element sub-array. Furthermore, the ASA operates in

6-dB backoff compared to the MSAs operation power. Based on Fig. 3.2, the digitization of the IF error signal, $e_{IF}(t)$, would require an ADC with a lower bit resolution than that of the ADC to sample $y_{IF}(t)$. It is worth noting that, in principle, the proposed scheme can be applied, to RF beamforming arrays. In this case, an additional dedicated RF chain (i.e., DAC and I/Q Mixer) would be required to generate the $-x(t)$ signal. However, the added hardware would constitute additional overhead and only serve the DPD training. This problem is avoided in hybrid-beamforming systems since the RF chains of the ASA can be used to generate the inverse signal, $-x(t)$.

3.1.1 Time Delay and LO Phase-Offset Callibration

In the hybrid beamforming architecture illustrated in Fig. 3.1, separate IQ mixers are used to generate the input signals fed to each of the sub-arrays. Given that the LO inputs to the mixers are typically generated by splitting a common LO source, it is important to ensure proper phase alignment between the IQ mixers LO inputs. Moreover, it is also important to compensate for any delay between the different RF paths. This is critical in guaranteeing optimal cancellation between the signals of the MSA and ASA. In order to identify the value ϕ_k of the phase-offsets of the different LO inputs, and the time delays t_d^k at the different RF paths, two complex baseband signals, $x_k(t), k = 1, ..., K = 2$, are generated to feed the two sub-arrays. Note that in this sub-section of the paper, both the MSA and ASA are operated in backoff. Let $C_{\tilde{x}_{k_1},\tilde{x}_{k_2}}(\tau)$ be the cross-correlation between $\tilde{x}_{k_1}(t)$ and $\tilde{x}_{k_2}(t)$ defined by

$$C_{\tilde{x}_{k_1},\tilde{x}_{k_2}}(\tau) = \int_{-\infty}^{+\infty} \tilde{x}_{k_1} \times \tilde{x}_{k_2}^*(t-\tau)dt. \tag{3.2}$$

The signals $\tilde{x}_k(t), k = 1, ..., K = 2$, are chosen such that: 1) the cross-correlation $C_{\tilde{x}_{k_1},\tilde{x}_{k_2}}(\tau)$ is small $\forall\tau$ and $k_1 \neq k_2$, 2) the auto-correlation $C_{\tilde{x}_k,\tilde{x}_k}(\tau)$ is large, has a positive real-value for $\tau = 0$, and decays quickly for $|\tau| > 0$. The complex baseband signals, $\tilde{x}_k(t), k = 1, ..., K = 2$, are generated in the discrete domain using multi-tones with random phases and magnitudes. The combined complex baseband output at the TOR, $\tilde{z}(t)$, can be written

as

$$\tilde{z}(t) = \sum_{k=1}^{K} G_k \tilde{x}_k(t - t_d^k) e^{-j(\phi_k + \phi_0)}, \tag{3.3}$$

where ϕ_0 is the phase-offset introduced by the down-converting mixer and G_k is the k^{th} sub-array gain. From (3.2) and (3.3), the cross-correlation coefficients between the received signal $\tilde{z}(t)$ and the k^{th} input signal, $\tilde{x}_k(t)$, can be computed as,

$$\begin{aligned} C_{\tilde{x}_k,\tilde{z}}(\tau) &= \int_{-\infty}^{+\infty} \tilde{x}_k \times \tilde{z}^*(t-\tau) dt \\ &= C_{\tilde{x}_k,\tilde{x}_k}(\tau + t_d^k) \times G_k e^{j(\phi_k+\phi_0)} + \sum_{\forall k' \neq k} C_{\tilde{x}_k,\tilde{x}_{k'}}(\tau + t_d^{k'}) \times G_{k'} e^{j(\phi_{k'}+\phi_0)}. \end{aligned} \tag{3.4}$$

Given that the cross-correlation between the different input signals $C_{\tilde{x}_k,\tilde{x}_{k'}}(\tau), k \neq k'$ is small, (3.4) can be approximated as:

$$C_{\tilde{x}_k,\tilde{z}}(\tau) \cong C_{\tilde{x}_k,\tilde{k}}(\tau + t_d^k) \times G_k e^{j(\phi_k+\phi_0)}. \tag{3.5}$$

Moreover, since $C_{\tilde{x}_k,\tilde{x}_k}(\tau + t_d^k)$ takes its maximum for $\tau + t_d^k = 0$ and decays quickly for $\left|\tau + t_d^k\right| > 0$, $C_{\tilde{x}_k,\tilde{z}}(\tau)$ is small for $\tau \neq -t_d^k$. the cross-correlation is (3.5) at $\tau = -t_d^k$ is

$$C_{-\tilde{x}_k,\tilde{z}}(t_d^k) \cong C_{\tilde{x}_k,\tilde{k}}(0) \times G_k e^{j(\phi_k+\phi_0)}. \tag{3.6}$$

Thus, from (3.5) it is clear that the time delay t_d^k of the different RF chains can be estimated by finding

$$t_d^k = -\underset{\tau \in \mathbb{R}}{\text{argmax}} \left| C_{\tilde{x}_k,\tilde{z}}(\tau) \right| \tag{3.7}$$

and from (3.7), the relative phase-offsets with respect to ϕ_1, $\Delta\phi_k = \phi_k - \phi_1$ can be given by:

$$\Delta\phi_k = \angle C_{\tilde{x}_k,\tilde{z}}(t_d^k) - \angle C_{\tilde{x}_1,\tilde{z}}(t_d^1). \tag{3.8}$$

To determine the time delay t_d^k and the relative phase-offsets $\Delta\phi_k$ accurately, the cross-correlation in (3.5) is approximated by using an up-sampled discrete time cross-correlation function

$$C_{\tilde{x}_k,\tilde{z}}[k] = \sum_{n=0}^{M'} \tilde{x}_k[n] \times \tilde{z}^*[n-k], \tag{3.9}$$

where M' is the length of the signal $\tilde{x}_k[n]$ and $\tilde{z}^*[n]$ after up-sampling. The up-sampling allows for fractional delay calibration and results in better cancellation of $x(t)$ in $y(t)$. The up-sampling ration used in the following thesis is $30:1$. Fig. 3.3 shows the measurement results of the received power versus phase-offset between the MSA and the ASA. Fig. 3.3 also provides an idea about how sensitive the combining is to the phase-offset calibration. Based on Fig. 3.3, it is also evident that the minimum received power is about 30 dB less than the maximum. This is particularly interesting as it indicates that the ASA will reduce the dynamic range at the TOR by almost 30 dB; hence, significantly reducing the required bit-depth of the digitizer. It is of note that while the derivation described above has been carried out for the LSMAS in Fig.1 (formed of two sub-arrays), it can be easily generalized for the case where the number of sub-arrays is greater that two, i.e. $K > 2$.

3.2 Validation Challenges: Definitions and Solution

In order to demonstrate the capacity of the proposed DPD to linearize an off-the-shelf mm-wave hybrid-beamforming array, an experimental test bed was developed. Due to the inability to modify the off-the-shelf beamforming array as necessary, i.e., to integrate the directional couplers needed to sample the PA outputs in Fig. 3.1, a far-field probing antenna was used in the proposed experimental test bed to capture the error signal $e(t)$. Hence, the probing antenna fulfils the functions of both the anti-beamforming modules and the out-of-phase combiner in Fig. 3.1. It is worth noting that the use of the far-field probing antenna to produce the error signal brings about additional challenges that are not present in the conceptual block diagram of Fig. 3.1. Those challenges needed to be mitigated to ensure accurate validation. For example, more than one ASA, operating linearly (in backoff to minimize the nonlinearity), is needed to transmit a sufficient amount of power to cancel the portion linearly related to $x(t)$ in $y(t)$ at the far-field probing antenna. For instance, if $K-1$ ASAs are available and used, each ASA is operated with backoff:

$$\text{Backoff [dB]} = 20 \times \log_{10}(K-1) \tag{3.10}$$

compared to the MSA. Furthermore, the DPD training algorithm presented in Section II assumed ideal transfer functions between the sub-arrays and the TOR. This assumption

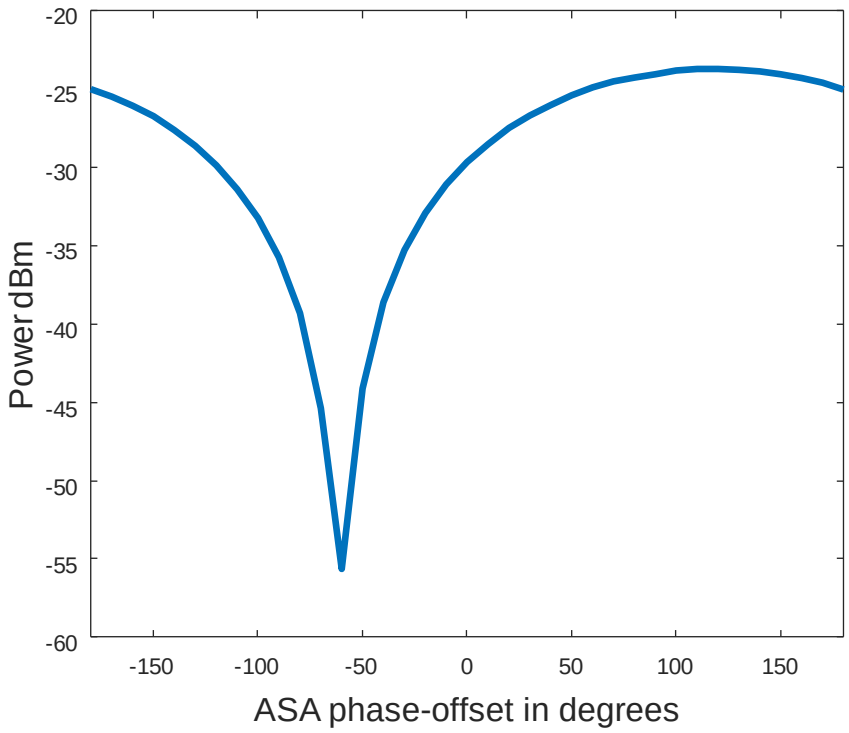

Figure 3.3: Received power at TOR with ASA turned on versus phase-offset.

does not hold in the validation test bed because i) the front ends of the MSA and ASAs may exhibit non-ideal frequency responses and ii) the error signal is obtained by combining the transmitted signals at a far-field receiving antenna after undergoing over-the-air propagation. Fig. 3.4 depicts the functional diagram of the proposed DPD scheme, including the impulse responses of the channels between the sub-arrays and the probing antenna as well as the corresponding baseband compensation blocks. In the following, the procedure devised to estimate the discrete baseband channel impulse responses is described.

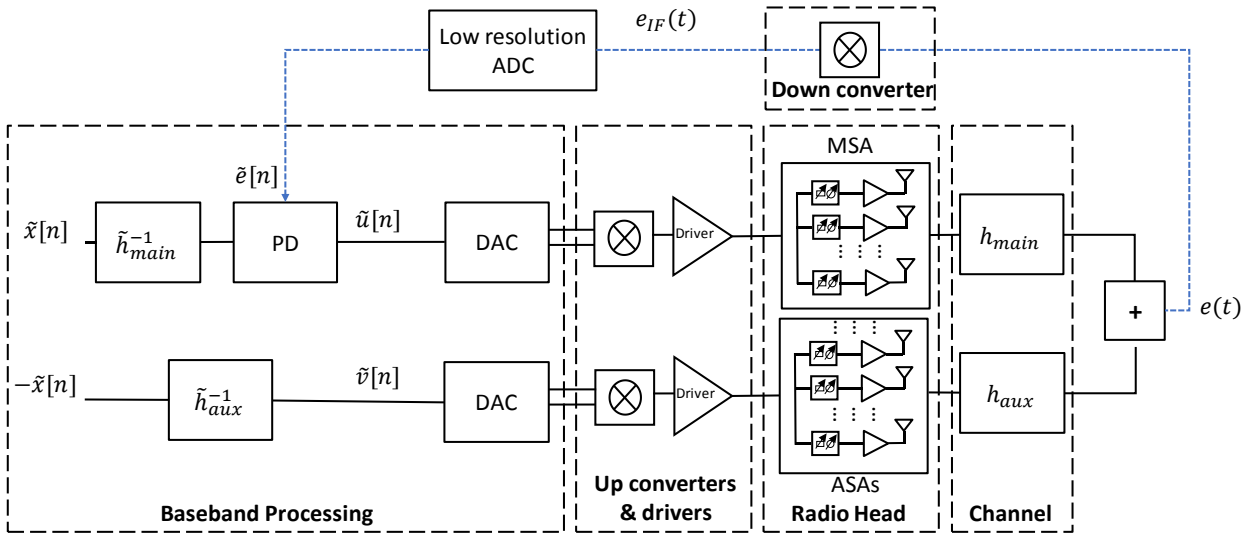

Figure 3.4: Functional diagram of proposed DPD system.

Channel Calibration

Let the discrete complex baseband equivalent of the channel impulse response between the MSA and the TOR be $\tilde{h}_{main}[n]$. Similarly, the channel impulse response between the k^{th} ASA and the TOR is denoted by $\tilde{h}_{ASA_k}[n]$. Hence, the combined response $\tilde{h}_{aux}[n]$ between the ASAs and the TOR can be expressed as

$$\tilde{h}_{aux}[n] = \sum_{k=1}^{K-1} \tilde{h}_{ASA_k}[n] \tag{3.11}$$

The channel impulse response of the MSA was estimated by operating the MSA in backoff (to avoid nonlinearities) and with non-radiating ASAs. Similarly, the channel impulse response of the ASAs was estimated with a non-radiating MSA. The complex baseband representations of the received signal corresponding to the MSA and ASAs at the TOR are then

$$\tilde{y}[n] = \left(\tilde{h}_{main} * \tilde{u}\right)[n] \tag{3.12}$$

and

$$\tilde{y}_{aux}[n] = \left(\tilde{h}_{aux} * \tilde{v}\right)[n] \tag{3.13}$$

respectively, where $\tilde{u}[n]$ is the signal transmitted by the MSA and $\tilde{u}[n]$ is the signal transmitted by the ASAs. Considering a complex channel response of length $P+1$ (i.e $\tilde{h}_{main}[n]=0$ for $n<0$ and $n>P$ and likewise $\tilde{h}_{aux}[n]=0$ for $n<0$ and $n>P$), (3.12) and (3.13) can then be written in matrix form as follows

$$\tilde{\mathbf{y}} = \mathbf{U}\tilde{\mathbf{h}}_{main} + \tilde{\boldsymbol{\epsilon}}_{main} \tag{3.14}$$

$$\tilde{\mathbf{y}}_{aux} = \mathbf{V}\tilde{\mathbf{h}}_{aux} + \tilde{\boldsymbol{\epsilon}}_{aux} \tag{3.15}$$

where $\tilde{\mathbf{h}}_{main} = \big(\tilde{h}_{main}[0], \big(\tilde{h}_{main}[1], \cdots, \big(\tilde{h}_{main}[P]\big)$, and likewise, $\tilde{\mathbf{h}}_{aux} = \big(\tilde{h}_{aux}[0], \big(\tilde{h}_{aux}[1], \cdots, \big(\tilde{h}_{aux}[P]\big)$, $\tilde{\boldsymbol{\epsilon}}_{main}$ and $\tilde{\boldsymbol{\epsilon}}_{aux}$ are the modelling errors in fitting $\tilde{\mathbf{h}}_{main}$ and $\tilde{\mathbf{h}}_{aux}$ respectively and $\mathbf{U}$ and $\mathbf{V}$ are the convolution matrices

$$\mathbf{U} = \begin{pmatrix} \tilde{u}[n] & \cdots & \tilde{u}[n-P] \\ \vdots & \ddots & \vdots \\ \tilde{u}[n-M+1] & \cdots & \tilde{u}[n-P-M+1] \end{pmatrix} \tag{3.16}$$

$$\mathbf{V} = \begin{pmatrix} \tilde{v}[n] & \cdots & \tilde{v}[n-P] \\ \vdots & \ddots & \vdots \\ \tilde{v}[n-M+1] & \cdots & \tilde{v}[n-P-M+1] \end{pmatrix} \tag{3.17}$$

where M is the length of the block of samples for $\tilde{u}[n]$ and $\tilde{v}[n]$ used in estimating the channels. The least-square estimates $\hat{\mathbf{h}}_{main}$ and $\hat{\mathbf{h}}_{aux}$ of the complex baseband channel impulse responses $\tilde{\mathbf{h}}_{main}$ and $\tilde{\mathbf{h}}_{aux}$, can then be written as

$$\hat{\mathbf{h}}_{main} = \big(\mathbf{U}^H\mathbf{U}\big)^{-1}\mathbf{U}^H\tilde{\mathbf{y}} \tag{3.18}$$

$$\hat{\mathbf{h}}_{aux} = \big(\mathbf{V}^H\mathbf{V}\big)^{-1}\mathbf{V}^H\tilde{\mathbf{y}}_{aux} \tag{3.19}$$

The use of different impulse responses to describe the channels of the MSA and ASAs is necessary because the non-ideal frequency responses of the sub-arrays may vary. The impulse response of the channel between MSA and the probing antenna, and its corresponding inverse, $\hat{h}^{-1}_{main}$, (shown in Fig. 3.4), are then used to rewrite the DPD basis matrix described in (2.17) as follows:

$$\tilde{\psi}_l\big(\tilde{\mathbf{x}}[n]\big) = \big(\hat{h}^{-1}_{main} * \tilde{x}\big)[n-m'_l]\Big|\big(\hat{h}^{-1}_{main} * \tilde{x}\big)[n-m_l]\Big|^{2p_l}, \tag{3.20}$$

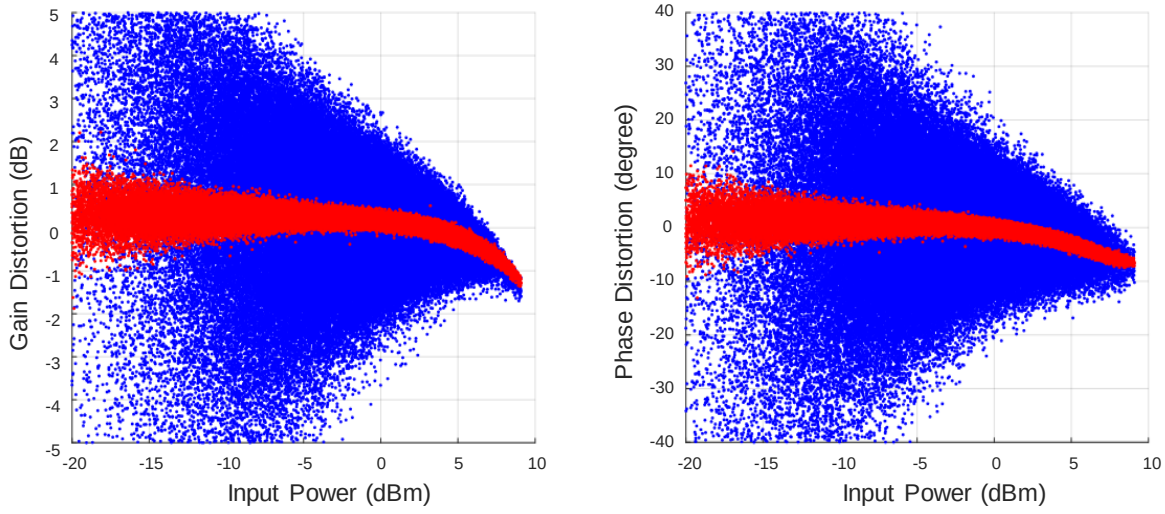

Figure 3.5: Left: MSA's AM/AM before (blue) and after (red) channel calibration. Right: MSA's AM/PM before (blue) and after (red) channel calibration.

where the inverse channel impulse response $\hat{h}_{main}^{-1}[n]$ is defined so that (3.21) is satisfied

$$\left(\hat{h}_{main}^{-1} * \hat{h}_{main}\right)[n] = \delta[n]. \tag{3.21}$$

Similarly, $\hat{h}_{aux}^{-1}[n]$ is used to pre-process the input signal to the ASAs so that the cancellation of $y_{aux}(t)$ from $y(t)$ is maximized. Thus the inverse, $\hat{h}_{aux}^{-1}[n]$, is determined so that (3.22) is satisfied

$$\left(\hat{h}_{aux}^{-1} * \hat{h}_{aux}\right)[n] = \delta[n]. \tag{3.22}$$

For illustration purposes, Fig. 3.5 shows the AM/AM and AM/PM characteristics of an MSA, when the ASAs are non-radiating, before and after pre-compensation for the channel response using $\hat{h}_{main}^{-1}[n]$, with impulse response length $P + 1 = 120$. Based of Fig. 3.5, one can deduce that the application of $\hat{h}_{main}^{-1}$ allowed for the de-embedding of the channel response, so that the AM/AM and AM/PM characteristics are focused on the MSA nonlinearity. This approach also enable the DPD coefficients to be more robust to the variation in the channel.

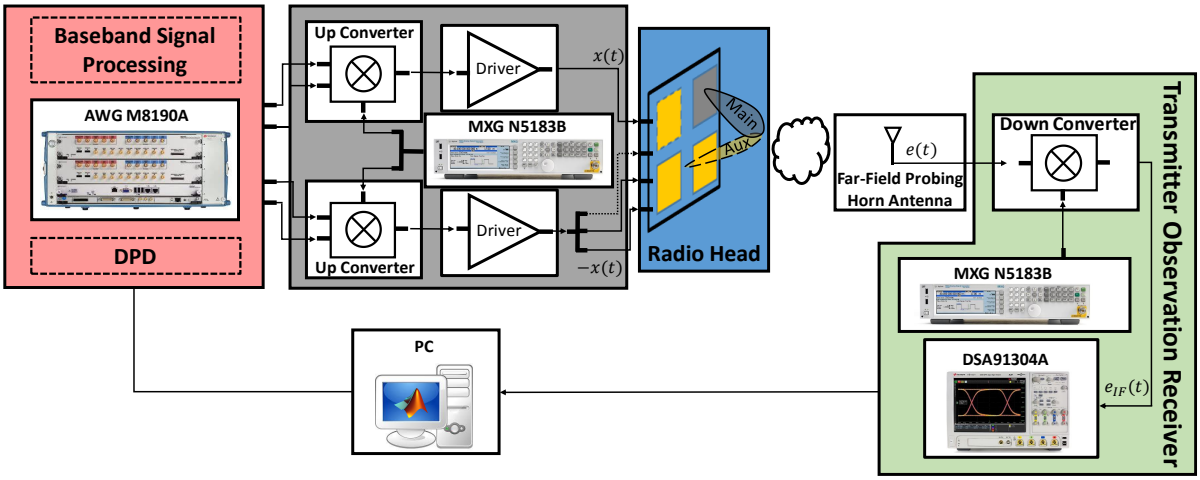

Figure 3.6: Block diagram of experimental setup with two alternate configurations of the radio head; three ASAs, and two ASAs.

3.3 Experimental Validation

3.3.1 Measurement Setup

The diagram shown in Fig. 3.6 depicts the measurement setup used to validate the proposed DPD system modeled in Fig. 3.4. The vector signal generation portion of the setup includes an arbitrary waveform generator (AWG, M8190A from Keysight Technologies) used to synthesize the test signals around an IF of 2.4 GHz. The IF signals are then up-converted to 28 GHz using an image-rejection IQ mixer (MMIQ1037H from Marki) and fed into an Anokiwave AWMF-0134 radio head [23] that includes the PAs, attenuators, phase shifters and four 64-element sub-arrays. Of the four sub-arrays, one was used as the MSA in this experiment and, depending on the experiment, two or three sub-arrays were used as ASAs. A receiving horn probing antenna was placed in the far-field and its out-put signal down-converted to an IF using a down-converting mixer (MM11140H from Marki). The received IF signal was then digitized and used to train the DPD function. The radio head was attached to a step motor to automatically control its relative angle to the receiving horn antenna. The experiments were conducted using two wideband OFDM signals of 200 MHz

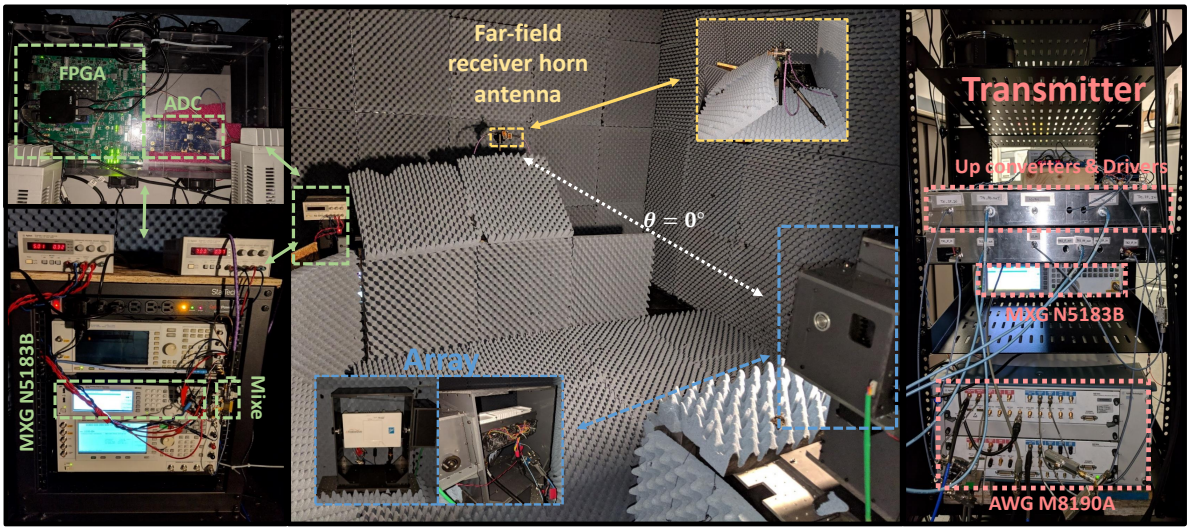

Figure 3.7: Photograph of measurement setup.

and 800 MHz bandwidths with subcarriers modulated using 256-QAM, sub-carrier spacing of 120 KHz, and characterized by a PAPR of 10 dB. The test signals sampling rates were 1 Gsps and 4 Gsps respectively. The setup shown in Fig. 3.7 was configured to allow for two experimental variations. Experiments used either two or three sub-arrays as ASAs that were operated at 6 dB and 9 dB backoff respectively. In order to ensure acceptable signal accuracy, the setup was calibrated using a wideband multi-tone signal with a 1 MHz tone spacing following the procedure described in [24]. Furthermore, LO phase-offset and channel impulse response characterization were performed using the theory described in the above sub-sections.

3.3.2 Measurement Results Using Three ASAs and 200 MHz Test Signal

In this variant, three sub-arrays were employed as ASAs and an OFDM signal with modulation bandwidth equal to 200 MHz was used as a test signal. The test signal was pre-processed to pre-compensate for the channel impulse response (channel between the MSA

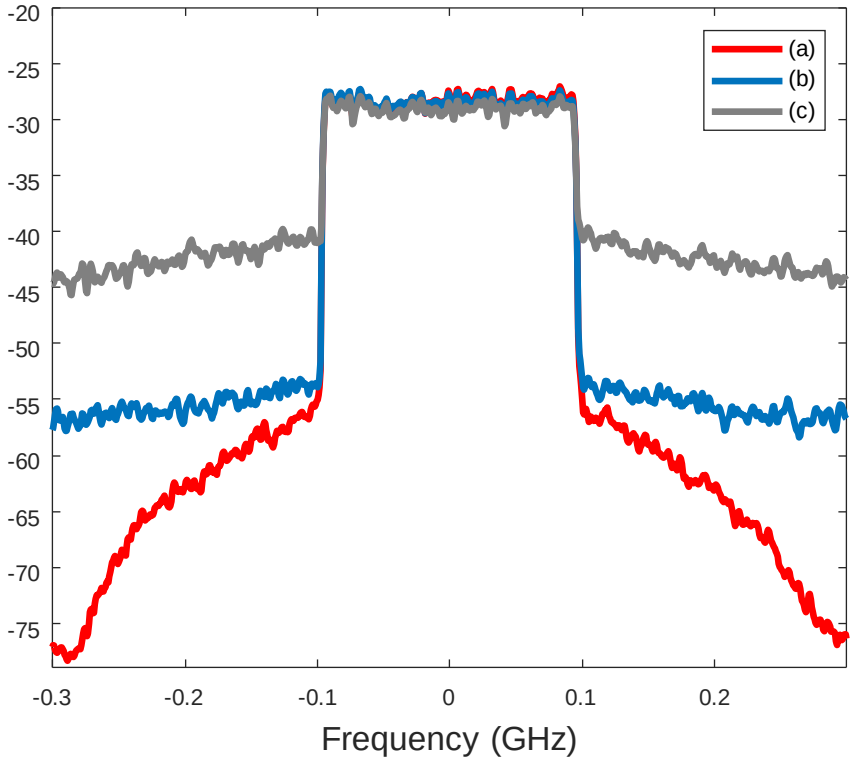

Figure 3.8: Far-field received signal for non-radiating ASAs without DPD using: (a) full 16-bit ADC resolution; (b) 4-bits ADC resolution; and (c) 2-bits ADC resolution.

and the probing antenna), and then fed as the RF input of the MSA (64-element) of the four 64-element radio head. The same test signal was also pre-processed to account for the LO phase-offset, time misalignment and channel impulse response (channel between the three ASAs and the probing antenna) before driving the three remaining sub-arrays. The resulting error signal captured by the far-field probing antenna was then used to identify the coefficients of the CRV-series based SISO DPD function. For that, the nonlinearity order, and nonlinear and linear memory depths were set to 5, 7 and 15 respectively, resulting in a total of 24 coefficients. It is of note that in this experiment, the nonlinear basis of the CRV expression of (2.17) was used, with even orders higher than two removed.

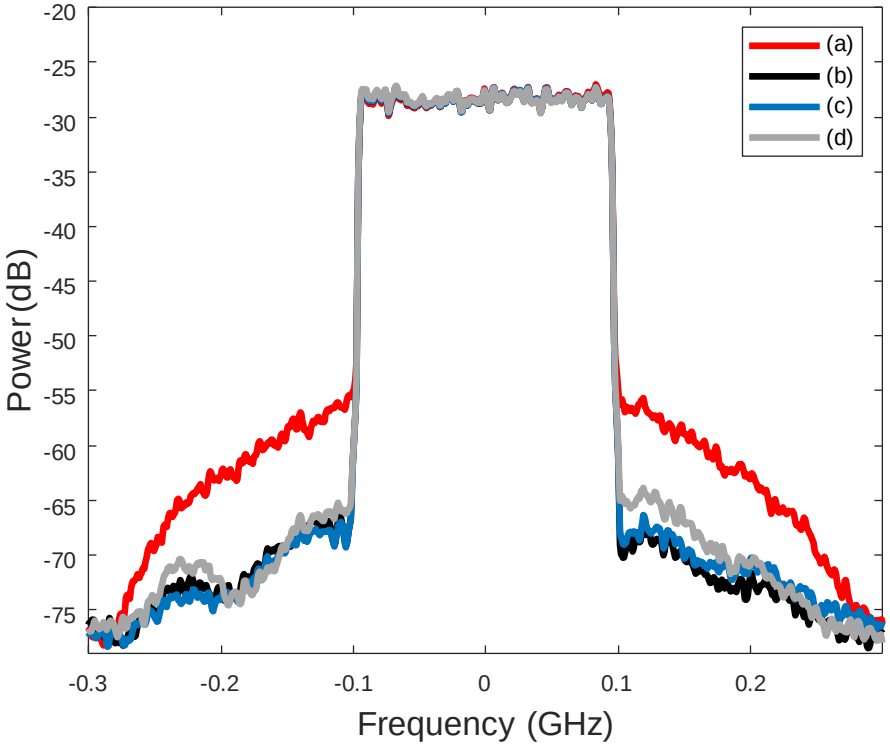

Figure 3.9: Far-field received signal spectrum (three-ASAs case): (a) before DPD; (b) after DPD with non-radiating ASAs and 16-bit ADC; (c) after DPD with radiating ASAs and 4-bit ADC; and (d) after DPD with radiating ASAs and 2-bit ADC.

Furthermore, the error signal was captured using an ADC (AD9208 from Analog Devices) with a sampling rate of 3 Gsps and 16-bit, 4-bit and 2-bit, and an analog bandwidth of 1.5 GHz. 3.8, illustrates the measured spectrum without DPD and with non-radiating ASAs. From Fig. 3.8; it is clear that the cases using a 4-bit and 2-bit ADC resolution imply a quantization noise in excess of the out-of-band distortion levels. This limited the ability of the resulting DPD to demonstrate any appreciable linearization. These problems were not encountered when the DPD was trained using a 16-bit resolution ADC as can be seen in Fig. 3.9-(b). However, when the ASAs were used during the DPD training (as can be deduced from Fig. 3.9), a 4-bit resolution ADC allowed for a reduction in the adjacent

channel power ratio (ACPR) from −33 to −43 dBc, and the error vector magnitude (EVM) dropped from 5.8% to 1.64%. These results are com-parable to the DPD performance with the non-radiating ASAs when using a full resolution receiver that achieved an ACPR of −42.3 dBc and EVM of 1.68% after DPD. According to Fig. 3.9, when a 2-bit ADC is used during DPD training, the linearization capacity was slightly reduced. The results in Fig. 3.9 show an improvement in ACPR from -33 to -41.8 dBc and in EVM from 5.8% to 2.1%.

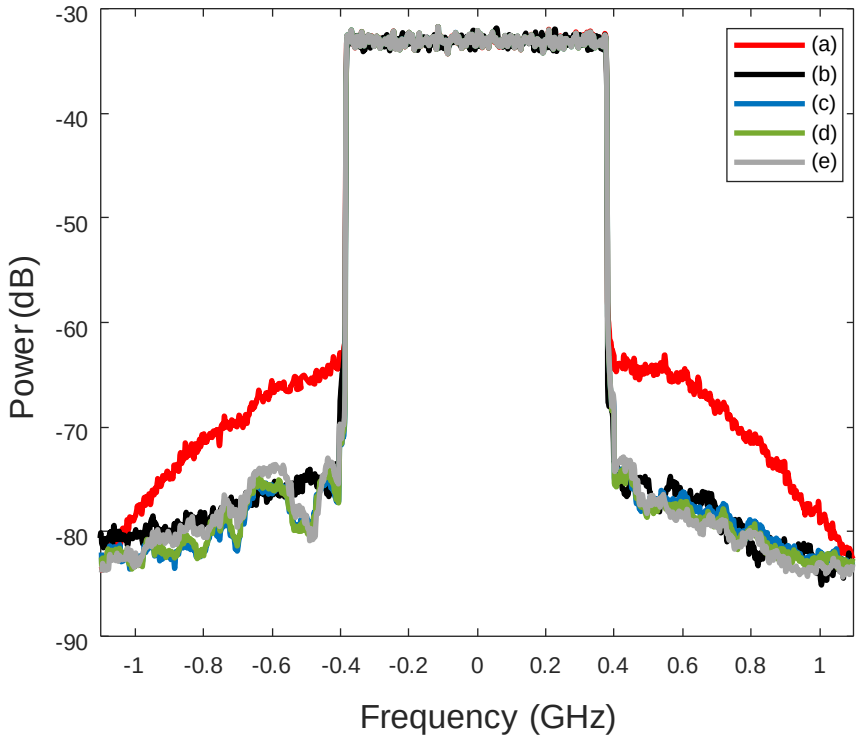

Figure 3.10: Far-field received signal spectrum (two-ASAs case): (a) before DPD; (b) after DPD with non-radiating ASAs; (c) after DPD with radiating ASAs and full resolution ADC; (d) after DPD with radiating ASAs and 4-bit ADC; (e) after DPD with radiating ASAs and 2-bit ADC.

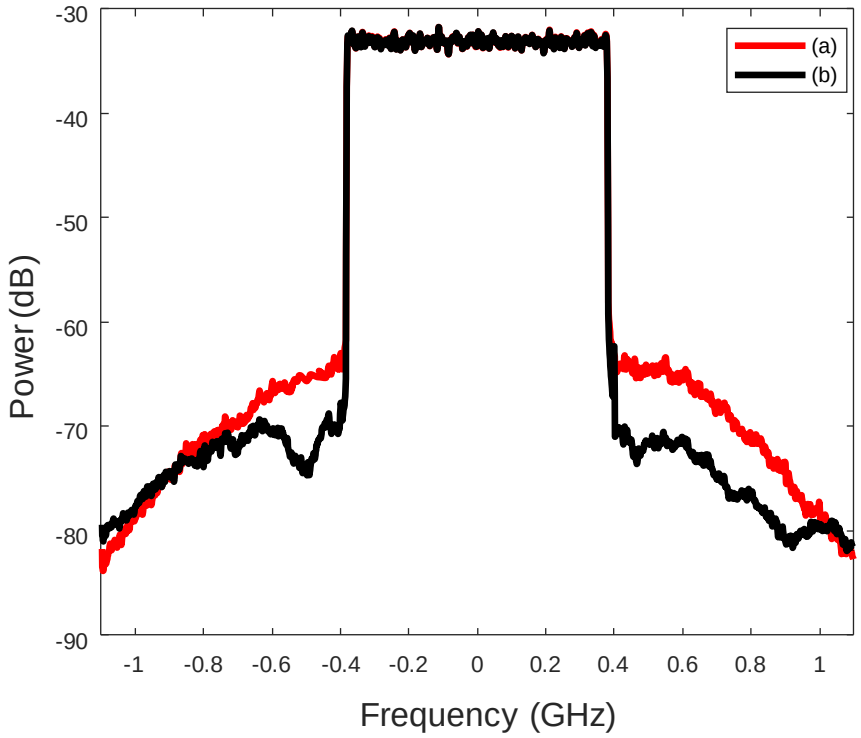

Figure 3.11: Far-field received signal spectrum (two-ASAs case): (a) before DPD; (b) after DPD with radiating ASAs and 1-bit ADC.

3.3.3 Measurement Results Using Two ASAs and 800 MHz Test Signal

In this variant, two sub-arrays are employed as ASAs and an OFDM signal with modulation bandwidth equal to 800 MHz was used as a test signal. Again, as in the first variant, the error signal captured by the probing antenna was used to identify the coefficients (even orders above two were re-moved) of the CRV-series based SISO DPD function. For that, the nonlinearity order, nonlinear and linear memory depths were set to 7, 9 and 0, respectively, resulting in a total of 13 coefficients. Note that during DPD training, the main beam

was directed towards the broadside and the error signal was captured using a high-speed oscilloscope (DSA91304A from Keysight Technologies) with resolution of 8-bit, 4-bit, 3-bit, 2-bit and 1-bit, analog bandwidth of 13 GHz, and sampling rate of 40 Gsps. Fig. 3.10 shows the spectrum captured at the probing antenna before and after application of the trained DPD function and with non-radiating ASAs. Based on Fig. 3.10, the application of the trained DPD allowed for a reduction of the ACPR and the EVM from -35 to -44 dBc and from 5.0% to 1.6%, respectively. These results were then compared to those obtained when the DPD was trained with non-radiating ASAs and using a full resolution (8-bit) digitizer. The results showed that the ACPR was reduced from -35 to -43 dBc, and the EVM from 5.0% to 1.7%. It is worth noting that the significant linearization capacity seen in Fig. 3.10 was obtained with different digitizer resolutions (i.e. full or 8-bit, 4-bit and 2-bit resolutions) and the EVM was maintained at 1.6%. This confirms that the digitizer resolution reduction enabled by the proposed DPD scheme did not com-promise the schemes linearization capacity. A 1-bit receiver was also tested and the linearization performance is depicted in Fig. 3.11. The results show that even a 1-bit receiver resolution was able to improve the ACPR by approximately 5 dB and decrease the EVM by half, from 5% to 2.5%. As with the first set of measurement results, it was shown that better results could be achieved by increasing the number of iterations for the training and by enabling auto-scaling.

3.4 Conclusions

A novel SISO DPD scheme using reduced receiver bit resolution to linearize the sub-arrays of a hybrid-beamforming array was proposed. Here, ASAs are mobilized to transmit an inverted version of the input signal to the MSA, the target to be linearized. Using anti-beamforming modules connected to the MSA and ASAs, the error signal needed for DPD training is generated. The input signal cancellation created by the weighted combining of the anti-beamforming module outputs results in a significant reduction of the required dynamic range for the TOR and consequently lowering the required ADC bit resolution. Experimental validation of the proposed DPD scheme using over the air combining showed excellent linearization capacity with only 4-bit resolution when applied to an array com-

prised of four 64-element sub-arrays operating at 28 GHz and when driven by 200 MHz modulated signals, and using a 2-bit resolution ADC when driven with 800 MHz signals.

Chapter 4

Single Set of DPD Coefficients Versus Steering Angles

In this chapter, a generalized SISO DPD scheme is introduced, where the DPD coefficients are trained using the signals captured at different steering angles. The measurement results of the proposed scheme are compared to the SISO DPD trained at $\theta = 0°$ and to the piece wise DPD approach in [5]. A systematic approach to predict the variation in RF beamforming arrays nonlinear behavior versus steering angles using an S-parameters based analysis is then presented and the effect of tapering on the PAs active load impedance variation is introduced. Afterward, the measurement result of a SISO DPD trained at $0°$ and the generalized SISO DPD trained using the signal captured at $\theta = 0°$, $\theta = 20°$ and $\theta = 40°$ of a 64-elements RF beamforming array with tapering applied are presented. Finally, the contributions and conclusions of this work are summarized.

4.1 Intoducrion

There have been some attempts, in the literature, to extend the application of DPD to multiple-antenna transmitter arrays. A conventional implementation of DPD technique, based on sub-6 GHz theory, is done in digital baseband and requires as many feedback

paths and predistorders as the number of power amplifiers. For the special case of RF beamforming, where a signal baseband transmission branch is connected to several PA and antenna elements, only a single DPD is expected to linearize the array of PAs. Different approaches have been investigated in the literature to linearize RF beamforming systems based a single-input-single-output (SISO) DPD modeling approach. In [25], the authors proposed a SISO DPD scheme to linearize RF beamforming arrays, in simulation, using all the PAs output signals. The DPD coefficients are trained to minimize the sum of the least squared errors of the different branches and is compared to the case where a single PA element is used to train the antenna array. A SISO beamforming oriented DPD is also introduced in [26, 19] where the DPD function is trained to linearize the main beam signal. In the proposed scheme, the PA outputs are sampled using direction couplers and utilizing a time-shared feedback path. The SISO DPD coefficients, in [26, 19], are then trained to minimize the sum of least square error of the PA outputs after the effect of analog beamforming coefficients are removed. Moreover, a SISO DPD for phased arrays using far-field probing antenna was proposed in [19, 18, 27], where the combined error signal at the far-field is minimized. In an attempt to reduce the variation between the PA nonlinear behaviour in phased arrays and linearize the array response in the main beam and the sidelobes, [28] proposed the use of analog tuners implemented before the PAs to compensate for the variation in the PA outputs between the different RF chains. Finally, the author in [20] used couplers at the PA outputs in conjunction with an anti-beamforming module, implemented in hardware, to cancel the beamforming weights and generate a far-field equivalent signal to train the SISO DPD function. One of the major issue that phased arrays suffer from is the angle dependent load modulation exhibited by the array at the PA outputs [29, 30, 31]. This is mainly due to the finite isolation between the antenna elements that causes the impedance seen by the different PAs to vary. Consequently, this causes the PAs to exhibit different nonlinear behaviour that is steering angle dependent. The authors in [27], showed in measurements that the linearization capacity of a single set of SISO DPD coefficients trained at broadside, was not maintained for different beamforming direction. In an attempt to tackle the challenges associated with the load modulation on the DPD linearization performance, the author in [27], proposed the use of a steering angle-dependent sets of DPD coefficients to linearize the array for

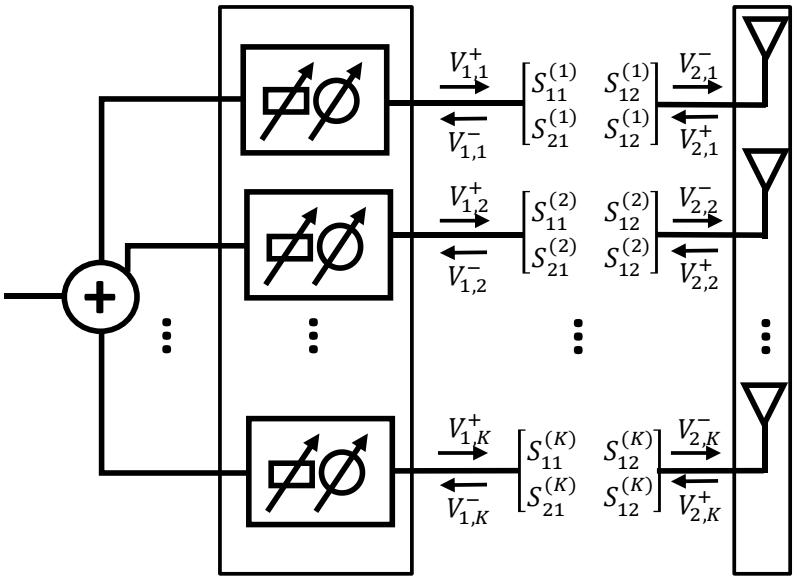

Figure 4.1: Block diagram of an RF beamforming array with K antenna elements and finite antenna cross-coupling.

different combination of beamforming directions. Using the scheme in [27], the authors demonstrated, in measurements, the capacity of three sets of DPD coefficients trained at $\theta = 0°$, $\theta = 20°$ and $\theta = 40°$ to linearize a 64-elements RF beamforming array at different directions using an 800 MHz Orthogonal frequency-division multiplexing (OFDM) and operated at 28 GHz. A dual input-solution was also proposed in [14, 1, 15, 16] to linearize phased arrays with antenna mismatch. Using this scheme the DPD function is trained using the forward and reverse waves at the PA outputs. The dual-input modeling approach demonstrated good linearization capability. The effect of the load modulation variation versus steering angles on the dual-input DPD did not, however, seen further investigation. It is hence, important to investigated the effect of the load modulation variation at different steering angles on the PAs nonlinear behaviour.

In this thesis, we propose to investigate the effect of the load modulation on the PAs nonlinear behaviour using an S-parameters based analysis. A single set of DPD coefficients,

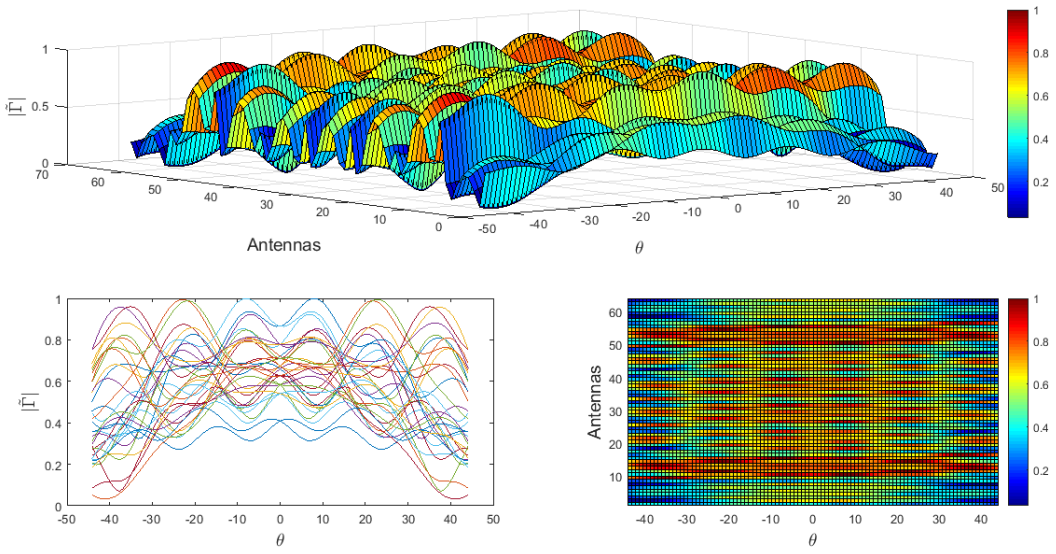

Figure 4.2: Normalized reflection coefficent, $\tilde{\Gamma}_k(\theta, \phi)$, at the antenna elements versus steering angles.

trained using signals captured at different steering angles to minimize the sum of the least squared error at different beamforming angles is then proposed. Finally, an analysis of the effect of tapering on the reflected power variation at the PA outputs and on the DPD linearization capacity are investigated.

4.2 Investigation of DPD linearization capacity over wide steering angels: with and without tapering

In order to compensate for the variation in the PAs nonlinear behaviour at different steering angles in RF beamforming arrays, the work in [5], suggested the use of multiple sets of DPD coefficients trained at different steering angles to linearize an RF beamforming array at different directions. As the array is steered, the appropriate set of trained DPD coefficients

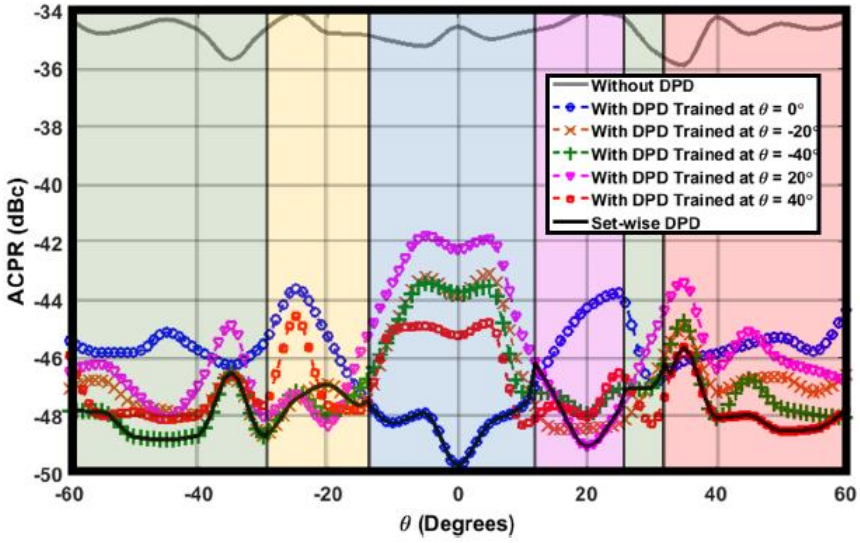

Figure 4.3: Measured ACPR of a 64-element array versus θ in [5].

are selected to linearize the array. The training angles used in [5], were selected where the ACPR before DPD showed the largest variation. The approach in [5] was able to minimize the EVM and ACPR variation for different steering angles. In this section, we will investigate the effect of the variation in the reflected power at the PA outputs on the array nonlinear behaviour and on the DPD linearization capacity.

Analyzing the effect of the load modulation on the array nonlinear behavior can be very challenging given the high dimensionality of the problem. Fig. 4.1, illustrate an RF beamforming array with K antenna elements where $V_{1,k}^{+}$ is the k^{th} PA input incident wave, $V_{2,k}^{-}$ and $V_{2,k}^{+}$ are the k^{th} antenna incident and reflect waves respectively, $V_{1,k}^{-}$ is the k^{th} PA input reflected wave and $S^{(k)} = \left[S_{11}^{(k)}, S_{12}^{(k)}, S_{21}^{(k)}, S_{22}^{(k)}\right]$ are the k^{th} PA S-parameters.

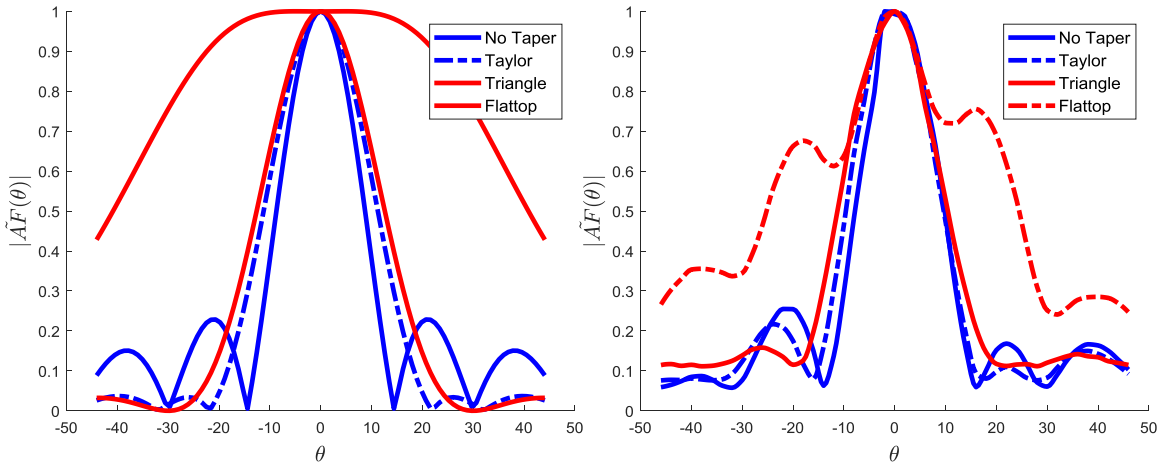

Figure 4.4: Radiation pattern with and without tapering applied on a 8×8 64-elements array; (Left) Simulation results; (Right) Measurement results.

Consequently, the k^{th} antenna incident wave can be expressed as follows:

$$\begin{aligned} V_{2,k}^{-} &= S_{21}^{(k)} V_{1,k}^{+} + S_{22}^{(k)} V_{2,k}^{+} \\ &= S_{21}^{(k)} V_{1,k}^{+} + S_{22}^{(k)} \sum_{i=1}^{K} S_{ki}^{A} V_{2,i}^{-} \\ &= S_{21}^{(k)} V_{1,k}^{+} + S_{22}^{(k)} \sum_{i=1}^{K} S_{ki}^{A} \big(S_{21}^{(i)} V_{1,i}^{+} + S_{22}^{(i)} \sum_{j=1}^{K} S_{ij}^{A} V_{2,j}^{-} \big) \\ &= S_{21}^{(k)} V_{1,k}^{+} + S_{22}^{(k)} \sum_{i=1}^{K} S_{ki}^{A} S_{21}^{(i)} V_{1,i}^{+} + S_{22}^{(k)} \sum_{i=1}^{K} S_{ki}^{A} S_{22}^{(i)} \sum_{j=1}^{K} S_{ij}^{A} V_{2,j}^{-} \end{aligned} \tag{4.1}$$

where S^A is the array coupling matrix. In order to simplify the recursive function described in Eqn. (4.1), we will assume that

$$S_{22}^{(k)} \sum_{i=1}^{K} S_{ki}^{A} S_{21}^{(i)} V_{1,i}^{+} \gg S_{22}^{(k)} \sum_{i=1}^{K} S_{ki}^{A} S_{22}^{(i)} \sum_{j=1}^{K} S_{ij}^{A} V_{2,j}^{-} \tag{4.2}$$

and second that the PAs S-parameters $S^{(k)}$ are identical for $k = 1, \cdots, K$. Consequently,

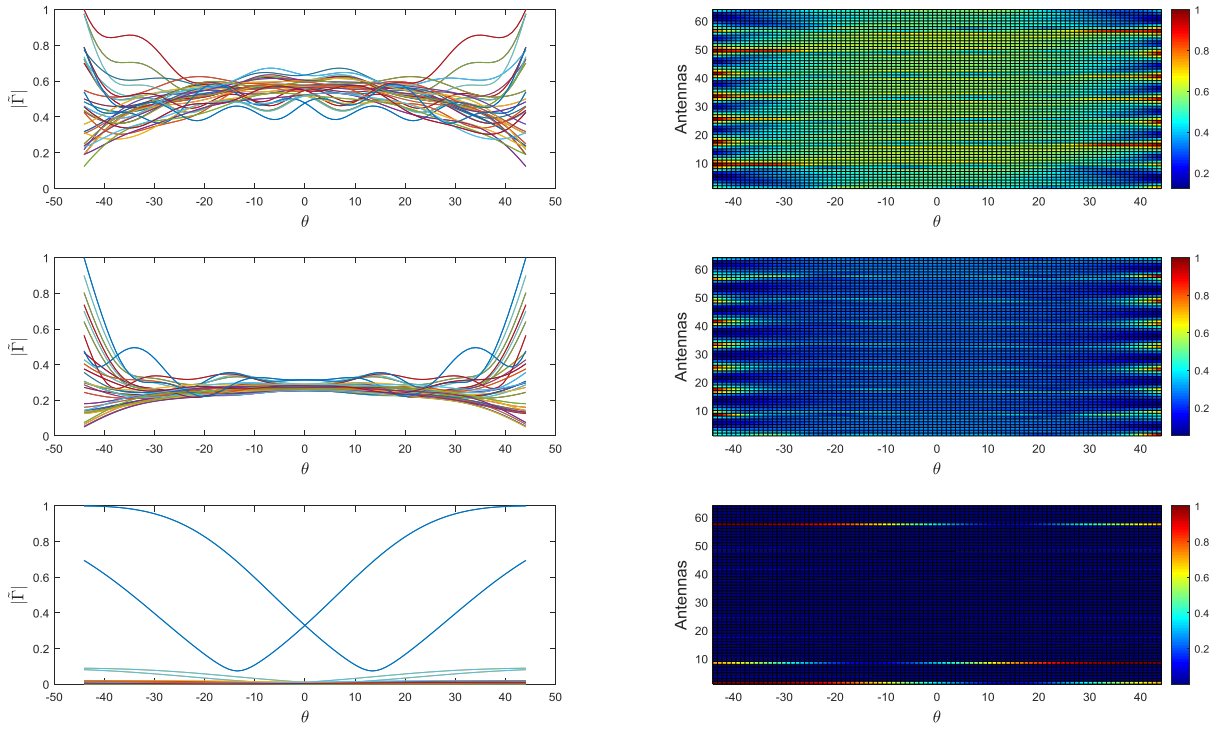

Figure 4.5: Normalized reflection coefficient, $\tilde{\Gamma}_k(\theta, \phi)$, at the antenna elements versus steering angles with tapering; (Top) Taylor window; (Middle) Triangle window; (bottom) Flat-top window.

Eqn. (4.1) can be rewritten as follows:

$$V_{2,k}^{-} = S_{21} V_{1,k}^{+} + S_{22} S_{21} \sum_{i=1}^{K} S_{ki}^{A} V_{1,i}^{+} \tag{4.3}$$

Apply the RF beamforming assumption,

$$V_{1,k}^{+}(\theta, \phi) = w_k e^{j\phi_k(\theta,\phi)}, \tag{4.4}$$

Eqn. (4.3) becomes:

$$V_{2,k}^{-}(\theta, \phi) = S_{21} w_k e^{j\phi_k(\theta,\phi)} + S_{22} S_{21} \sum_{i=1}^{K} S_{ki}^{A} w_i e^{j\phi_i(\theta,\phi)} \tag{4.5}$$

where w_k and $\phi_k(\theta,\phi)$ are the k^{th} chain tapering and beamforming coefficients. The far-field equivalent received signal, $r(\theta,\phi)$ can hence be expressed as follows:

$$\begin{aligned} r(\theta,\phi) &= \sum_{k=1}^{K} \alpha V_{2,k}^{-}(\theta,\phi) e^{-j\phi_k(\theta,\phi)} \\ &= \sum_{k=1}^{K} \alpha S_{21} w_k + \alpha S_{22} S_{21} \sum_{k=1}^{K}\sum_{i=1}^{K} S_{ki}^{A} w_i e^{j(\phi_i(\theta,\phi)-\phi_k(\theta,\phi))} \end{aligned} \tag{4.6}$$

where $\alpha \in \mathbb{R}$ is a normalization factor that includes the transmitting and receiving antennas efficiency and the propagation loss. Contrary to the ideal scenario without coupling and cross-talk, the user received signal, described by (4.6), depends on the beam-steering angle (θ,ϕ). From (4.6), it is also clear that the effect of the load-modulation at different steering angles takes the form a 2-D Fourier transform. In order to analyze the impact of the load modulation on the individual antenna PA elements and on the overall array we can define the reflected coefficient,$\Gamma_k(\theta,\phi)$, at the k^{th} antenna element as:

$$\Gamma_k(\theta,\phi) = \sum_{i=1}^{K} \frac{S_{ki}^{A} w_i e^{j(\phi_i(\theta,\phi)}}{w_k e^{j(\phi_k(\theta,\phi)}} \tag{4.7}$$

We also define the normalized reflected coefficient at the k^{th} antenna element, $\widetilde{\Gamma}_k(\theta,\phi)$, as follows:

$$\widetilde{\Gamma}_k(\theta,\phi) = \frac{\Gamma_k(\theta,\phi)}{\max\big(\Gamma_k(\theta,\phi)\big)} \tag{4.8}$$

Fig. 4.2, illustrates $\big|\widetilde{\Gamma}_k(\theta,\phi)\big|$ for $\phi = 0^\circ$ and $\theta \in [-45^\circ, 45^\circ]$ using an 8×8 array with lattice spacing $d_x = d_y = \lambda/2$ at 28 GHz. Due to the unavailability of an 8×8 EM simulated array, the S-parameters used in Fig. 4.2 were generated using the infinite array analysis, using the assumption that the coupling characteristics is the same in both the E and H plane and that the radiation pattern of each individual patch antenna is isotropic. The array S-parameter, S_{mn}^{A}, are then expressed as follows:

$$S_{mn}^{A} = \frac{c}{d_{mn}} e^{jkd_{mn}}, \tag{4.9}$$

and

$$S_{nn}^{A} = 0. \tag{4.10}$$

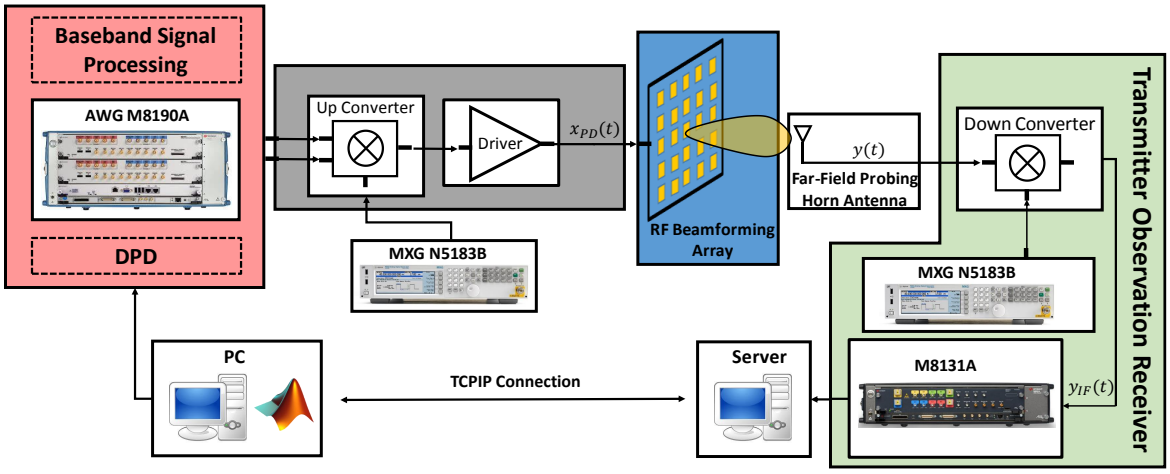

Figure 4.6: Measurement setup block diagram

From Fig. 4.2 we can observe a variation in the magnitude of the antennas reflection coefficient versus steering angles. This would induce a variation in the in the reflected power at the PA outputs that would theoretically impact the PAs inter-modulation distortion (IMD3) and cause the ACPR to vary versus steering angles. Fig. 4.3 illustrates the measured ACPR before and after DPD on a 64-elements RF beamforming array [23] measured in [5]. From the measurement results in Fig. 4.3, we can clearly see that the ACPR before DPD follows a similar behaviour as the simulated results in Fig. 4.2.

From (4.8), it is also evident that the reflection coefficient at the PAs port-2 are dependent of the tapering coefficients. This calls for the investigation on the effect of tapering on the reflection coefficients versus steering angles. This is remindful to the concepts used in the transmission line matching theory where tapering is commonly used to improve the matching bandwidth, however in the case of phased arrays the tapering has a spacial impact on the variation of the reflection coefficients versus steering angles. Hence, it is important to study if tapering could be used to reduce the variation of $\left|\Gamma_k(\theta,\phi)\right|$ at different beamforming directions. This is even more relevant, since tapering can also be used to shape the array factor, i.e, reduce the sidelobes and synthesize broader beam patterns, and consequently, is expected to be used on commercial phased arrays. Fig. 4.5, illustrates the effect of three different tapers on the magnitude of the active reflection coefficient at the

antenna elements, $\left|\tilde{\Gamma}_k(\theta,\phi)\right|$, for $\phi = 0°$ and $\theta \in [-45°, 45°]$, and on an 8×8 64-elements RF beamforming array. Fig. 4.4 (Left) illustrate the simulated radiation pattern of the used tapers. It is clear from Fig. 4.5 that applying tapering helped reduce the variation in $\left|\Gamma_k(\theta,\phi)\right|$ versus steering angles. This theoretically, would help reduce the variation in the array nonlinear behavior versus steering angles and enables the DPD coefficients to be more robust to the variation in the beamforming direction.

4.3 Theoretical formulation of the proposed DPD scheme

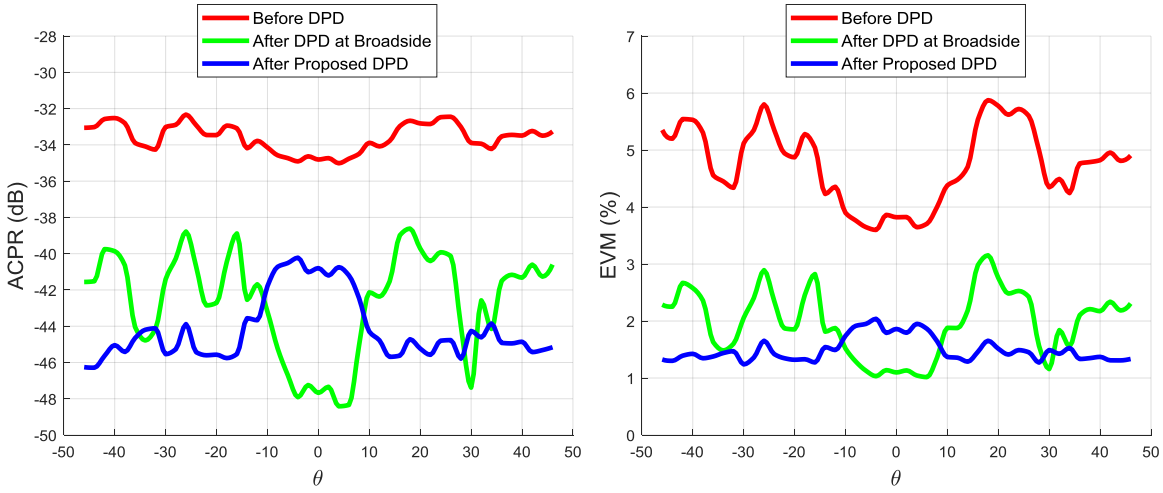

Figure 4.7: Measurement results of the ACPR (Left) and EVM (Right) before and after DPD trained at broadside and using signals captured at $\theta = 0°$, $\theta = 20°$ and $\theta = 40°$.

4.3.1 Proposed DPD formulation

Due to the variation in the load modulation at the PA outputs, the work in [27] demonstrated that a single set of DPD coefficients trained at broadside is not sufficient to linearize the array at different steering angles. In this section, we propose a novel DPD scheme

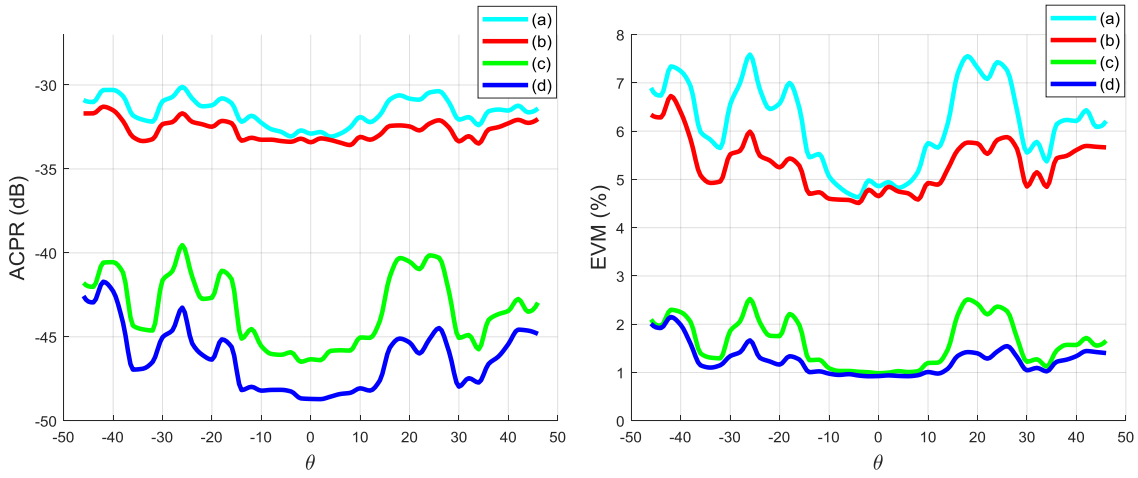

Figure 4.8: Measurement results of the ACPR (Left) and EVM (Right) before and after DPD trained at broadside; (a) Before DPD and without tapering; (b) Before DPD and with taper setting 1; (c) After DPD, without tapering and with average power of -28.8 dBm; (b) After DPD, with taper setting 1 with average power of -28.94 dBm.

trained that aims to minimize the variation in ACPR and EVM after DPD using a single set of DPD coefficients. Using this scheme the DPD function is trained using the captured error signal at different steering angles where the reflected power at the PA outputs shows significant variation and using the theory described above.

The error signal is denoted $\tilde{e}[n;\theta]$ where θ is the steering angle used to generate the error signal for training. The set of all possible steering angles for training purposes is denoted $\boldsymbol{\theta_T}$. Given $\tilde{x}[n]$ and $\tilde{e}[n;\theta]$ for $n = n_k, ..., n_k + N - 1$ and $\theta \in \boldsymbol{\theta_T}$, the update direction $\Delta\mathbf{C}^{(k)}$ of the predistortion model coefficients for the k^{th} iteration of DPD training is the direction that minimizes the squared l_2 norm, i.e, that minimizes

$$J = \sum_{\theta\in\boldsymbol{\theta_T}} \sum_{n=n_k}^{n_k+N-1} \left| \tilde{e}^{(k)}[n;\theta] - \sum_{l=1}^{L} c_l^{(k)} \psi_l\big(\tilde{\mathbf{x}}[n]\big) \right|^2 \tag{4.11}$$

and is determined with a standard least-square fit, with the solution

$$\Delta\mathbf{c}^{(k)} = \frac{1}{|\boldsymbol{\theta}_T|} \big(\Psi(\tilde{\mathbf{x}})^H \Psi(\tilde{\mathbf{x}})\big)^{-1} \Psi(\tilde{\mathbf{x}})^H \sum_{\theta\in\boldsymbol{\theta}_T} \tilde{\mathbf{e}}_i^{(k)}(\theta). \tag{4.12}$$

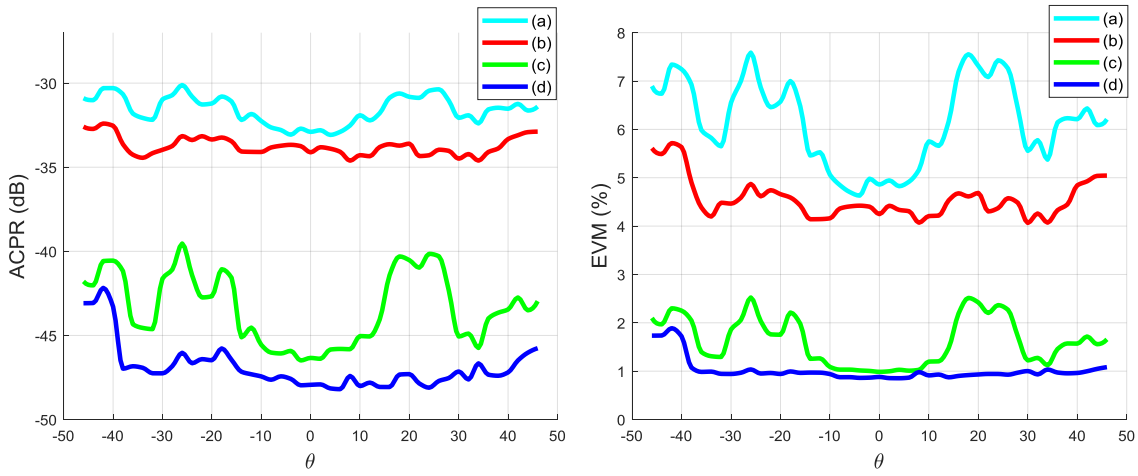

Figure 4.9: Measurement results of the ACPR (Left) and EVM (Right) before and after DPD trained at broadside; (a) Before DPD and without tapering; (b) Before DPD and with taper setting 2; (c) After DPD, without tapering and with average power of -28.8 dBm; (b) After DPD, with taper setting 2 with average power of -31.94 dBm.

Hence, by capturing the signal at different beamforming angles and using (4.12), the proposed generalized DPD function that minimize the variation in the NMSE and consequently the EVM is trained.

4.4 Measurement results

The diagram shown in Fig. 4.6 depicts a system block diagram of the measurement set up used to validate the proposed DPD scheme. The vector signal generation portion of the setup includes an arbitrary waveform generator (AWG, M8190A from Keysight Technologies) used to generate the test signals around an IF of 1.7 GHz. The IF signal is then up-converted to 28 GHz and fed to an 8×8 64-elements RF beamforming array that includes the PAs, the antennas and the digital phase shifters to steer the beams and has an EIRP at 1-dB compression point of 50 dBmi. A far-field receiving horn antenna is used to capture the training signal. A digitally controlled motor is used to align the beam

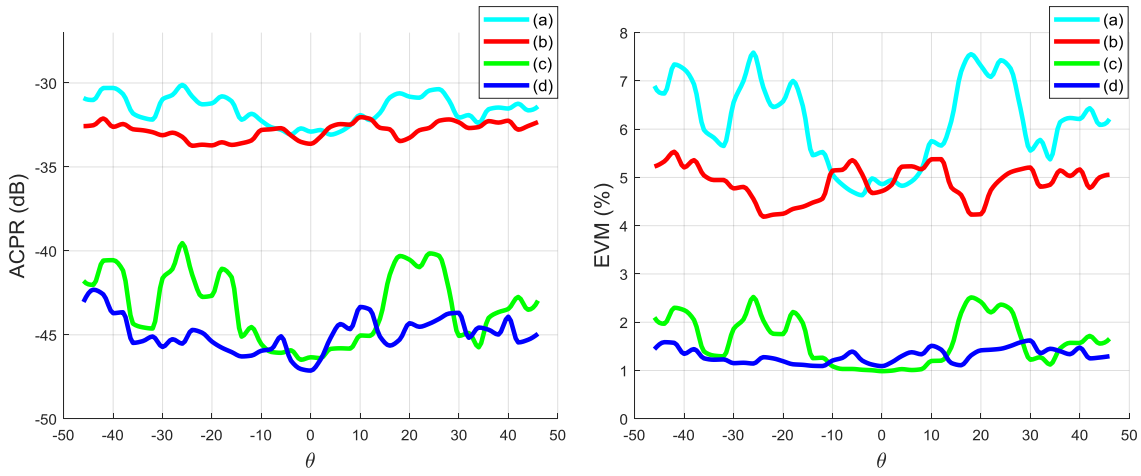

Figure 4.10: Measurement results of the ACPR (Left) and EVM (Right) before and after DPD trained at broadside; (a) Before DPD and without tapering; (b) Before DPD and with taper setting 3; (c) After DPD, without tapering and with average power of -28.8 dBm; (b) After DPD, with taper setting 3 with average power of -37.76 dBm.

with the receiver to capture the training signal and maximize the received power. The far-field signal is then down-converted to IF using a down-converting mixer (MM11140H from Marki). The received IF signal is then digitized using a digitized (M8131A from Keysight). The measurements were conducted using a 400 MHz wideband OFDM signal with subcarriers modulated using 256-QAM, sub-carrier spacing 120 KHz and characterized by a PAPR of 11 dB. In order to ensure a good signal accuracy, the setup was calibrated using a wideband multi-tone signal with 1 MHz tone spacing following the procedure in [24]. The DPD nonlinearity order, and nonlinear and linear memory depths were set to 9, 9, and 0 respectively, resulting in a total of 25 coefficients.

4.4.1 Case 1: No tapering

The training angles used to capture the signals needed to train the CRV-series based SISO DPD function are $\boldsymbol{\theta}_T = \{0°, 20°, 40°\}$. Note that during the DPD training, the main beam

was directed towards 0°, 20° and 40° in that order and the motor was used to align the main beam with the receiving horn antenna at each training angle before capturing the signal. Fig. 4.7 (Left) and Fig. 4.7 (Right) show the ACPR and EVM before and after DPD versus steering angles using a single SISO DPD trained at $\theta = 0°$ and the proposed scheme trained using the signals captured at $\theta \in \boldsymbol{\theta}_T$ respectively. The results from Fig. 4.7 (Left) and Fig. 4.7 (Right) show that the SISO DPD trained at $\theta = 0°$ was able to improve the ACPR from -35 to -48 dBc and the EVM from 4% to 1.1% at $\theta = 0°$, those results did not generalize well versus steering angles. For example at $\theta = 25°$ the ACPR only improved by 5 dB and the EVM was only reduced from 5.5% to 3%, hence the SISO DPD trained at $\theta = 0°$ is not enough to maintain an EVM below 2% for different steering angles. Those results are consistent with the results in [5]. In contrast to the SISO DPD trained at $\theta = 0°$, the proposed DPD was able to improve the ACPR from -34 to -45 dBc and the EVM from 6% to 1.4% for a wide range of steering angles, i.e. from $-45°$ to $-15°$ and from 15° to 45°. Using the proposed scheme, the EVM was maintained below 2% across all the steering range. The proposed DPD, however, was not enough to maintain the ACPR below -45 dBc for different steering angles, i.e. from $-15°$ to 15°. In order to maintain the EVM and ACPR below 2% and -45 dBc respectively, the peace-wise DPD in [5] provides better results versus steering angles when compared to proposed scheme.

4.4.2 Case 2: With tapering

Tapering can help reduce the sidelobes or to synthesize a wider beam pattern, this, however, comes at the expense of reduced array gain and can be further illustrated in Fig. 4.4 that shows the measured radiation pattern of the Anokiwave AWMF-0128 64-elements radio head [32] with and without tapering applied. In this measurement subsection, the DPD function is trained at broadside with different tapers and with the input average power to the array varied to keep a constant starting ACPR.

Fig. 4.8 (a) and (c) show the ACPR and EVM before and after DPD respectively and without tapering applied. The DPD in Fig. 4.8 was trained at broadside and with an average received power of -28.54 dBm. From Fig. 4.8 the ACPR and EVM were improved from -33 to -46 dBc and from 5% to 1% respectively at broadside. As expected

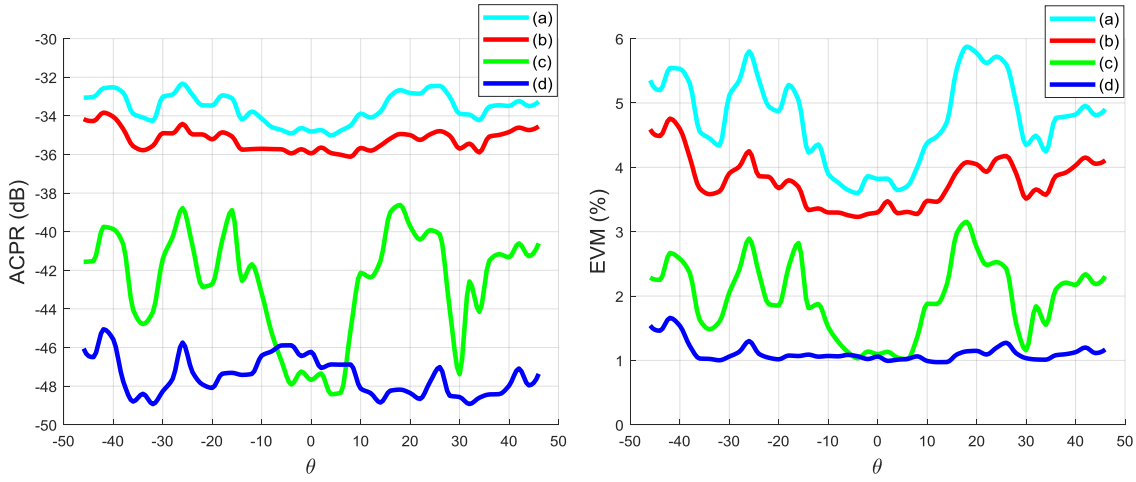

Figure 4.11: Measurement results of the ACPR (Left) and EVM (Right) before and after DPD trained at broadside and with the proposed DPD trained using signals captured at $\theta = 0°$, $\theta = 20°$ and $\theta = 40°$; (a) Before DPD and without tapering; (b) Before DPD and with taper setting 1; (c) After DPD trained at broadside and without tapering; (b) After proposed DPD and with taper setting 1.

the DPD performance is not maintained versus steering angles where the ACPR and EVM deteriorate to -39.5% and up to 2.6% respectively. Those results will be used as a reference in studying the effect of tapering on the ACPR and EVM before and after DPD. Fig. 4.8 (b) and (d) illustrate the DPD results with taper 1 applied and at a received power of -28.94 dBm. From Fig. 4.8, the ACPR and EVM were improved from -33 to -48.7 dBc and from 5% to 0.9% respectively at $\theta = 0°$. The ACPR and EVM where maintained below -43.2 and 1.65% from $-35°$ to $45°$ and below -41.7 dBc and 2% for the whole steering range. Using Taper 2 in Fig. 4.9 (b) and (d) the received power was further reduced to -31.9 dBm. Using this configuration, the measurement results show that the ACPR was reduced from -33.8 to -48 dBc and the EVM from -4.5% to 0.85% at $\theta = 0°$. The ACPR and EVM were maintained below -46 dBc and 1% from $-38°$ to $45°$ and below -42.3 dBc and 1.8% from $-45°$ to $45°$. Finally, using the flat-top taper, the received power was measured to be -37.76 dBm. Using taper 3 and from Fig. 4.10 (b) and (d), it is clear that the ACPR and EVM were reduced from -33 to -47 dBc and from 5% to 1.1% respectively at the

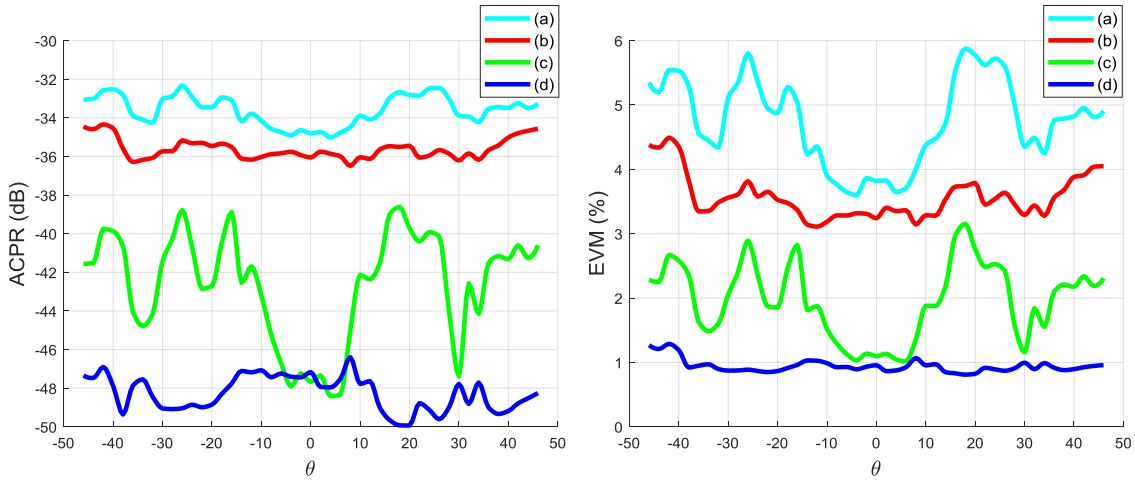

Figure 4.12: Measurement results of the ACPR (Left) and EVM (Right) before and after DPD trained at broadside and with the proposed DPD trained using signals captured at $\theta = 0°$, $\theta = 20°$ and $\theta = 40°$; (a) Before DPD and without tapering; (b) Before DPD and with taper setting 2; (c) After DPD trained at broadside and without tapering; (b) After proposed DPD and with taper setting 2.

angle, $\theta = 0°$, where the DPD was trained. The ACPR and EVM were maintained below -43 dBc and 1.6% for the full steering range.

Better results were measured when using the generalized SISO DPD proposed above in combination with tapering. Fig. 4.11 (b) and (d), shows the results of the proposed generalized DPD with tapering 1 applied. The received power in this case was -30.6 dBm compared to -29.4 dBm without tapering in Fig. 4.11 (a) and (c) for the same starting ACPR. From Fig. 4.11 (b) and (d), it is clear that the ACPR was improved by 10 to 14 dBc from -35 to at worst -45 dBc and at best -49 dBc and the EVM was improved from at worst 5% to at worst 1.6%. It is important to note that the EVM was maintained below 1.2% from $-38°$ to $45°$. Finally, using taper 2, the received power was -32.6 dBm. The results from Fig. 4.12 (b) and (d), show that using the proposed generalized DPD trained at $\theta = 0°, 20°, 40°$, the ACPR was improved from -35.5 to at worst -46.4 dBc and at best -50 dBc and the EVM improved from at worst 4.5% to at worst 1.2% and at best 0.85%.

The EVM was maintained below 0.95% from $-39°$ to $45°$.

4.5 Conclusions

In this Chapter, a generalized DPD scheme trained using the captured signal at different steering angles was introduced. Using this scheme, we showed that the EVM was able to be maintained below 2%. The proposed DPD was then compared to the SISO DPD trained at $\theta = 0°$ and to the peace-wise DPD in [5]. Afterward, the variation of the array nonlinear behavior was analyzed. The analysis lead to show that the load modulation is dependent on the steering angle and on the tapering coefficients. It was then demonstrated that tapering can be used to minimize the load modulation variation versus different steering angles. To confirm the simulation results, DPD measurement on a commercial 64-elements RF beamforming array were introduced. The measurement results, showed that using tapering the ACPR before DPD showed less variation compared to the case where no tapering is applied and that a SISO DPD trained at broadside was enough to linearize the array at different beamforming angles. Finally, the measurement result using the proposed generalized SISO DPD scheme with tapering applied showed further improvement in the EVM and ACPR versus steering angles.

Chapter 5

Conclusion

In this thesis, the practical deployment of DPD solutions for mm-wave phased arrays was studied. First, a power consumption reduction technique was introduced, then the load modulation effect on the array nonlinear behavior at different beamforming angles was analyzed and finally, a generalized DPD scheme, and a tapering assisted DPD were devised and demonstrated capacity to linearize a commercial array in different steering directions. Hence, by minimizing the DPD power consumption and reducing the DPD complexity using tapering and the proposed generalized DPD scheme, a practical implementation of DPD on phased arrays was devised.

In Chapter 2, we saw how mm-wave phased arrays can be used to mitigate the effect of the increase of free space path loss at higher frequencies. We then introduced the concept of tapering and it effect on array factor and on sidelobes levels. We then discussed the tradeoff between linearity and power efficiency in PAs and proposed DPD as a method to increasing the efficiency and allow the array to operate further in its non-linear region where the PAs are most efficient. Finally, we discussed the power consumption and complexity issues with the existing DPD solutions in the literature.

In Chapter 3, a novel SISO DPD scheme using reduced receiver bit resolution to linearize hybrid-beamforming arrays was proposed. A conceptual solution as well as a more practical implementation of the proposed scheme was introduced. Challenges with real life deployment of this DPD solution, like LO phase-offset cancellation and channel calibra-

tion were also discussed. Experimental validation of the proposed DPD scheme using a 4-bit resolution when applied to commercial array comprised of four 64-element sub-arrays operating at 28 GHz and when driven by 200 MHz modulated signals, and using a 2-bit resolution ADC when driven with 800 MHz signals were presented.

In chapter 4, we proposed a generalized SISO DPD scheme to linearize RF beamforming arrays and minimize the EVM variation versus steering angles. The measurement results of the proposed scheme were then compared to the SISO DPD trained at broadside and to the peace-wise DPD in [5]. The proposed scheme showed robustness to the load modulation variation at different steering angles and was able to maintain an EVM below 2%. A theoretical analysis of the effect of the load modulation on RF beamforming arrays was then introduced. The analysis lead to the conclusion that the load modulation is dependent on the steering angles and on the tapering coefficients. The effect of tapering on a 16-elements EM simulated and on a 64-elements Matlab simulated array was then investigated and the findings showed that applying certain tapers could decrease the variation in the load modulation and hence reduce the variation in the ACPR and EVM versus steering angles. The simulation results were further confirmed using the measurement results on a 64-elements commercial RF beamforming array that proved that the tapering help reduce the ACPR variation, before and after DPD, in different beamforming directions. The results also showed that a SISO DPD function trained at broadside was enough to linearize the 64-elements array. Finally, the proposed generalized DPD scheme was used to linearize the array with tapering applied. The results showed even further improvements to the ACPR and EVM results.

5.1 Future work

The ultimate goal of this work was to demonstrate that a low complexity low power consumption DPD is feasible under real-world measurement conditions and has the potential to be practical in commercial deployments. The presented work demonstrated the capacity of tapering to reduce the load modulation variation for different beamforming angles and that a SISO DPD trained at broadside in conjuncture with tapering or a DPD trained

using the signals captured at different angles was enough to linearize RF beamforming arrays, however there are many practical considerations that need further investigation. This includes the following avenues below.

Open-loop vs closed-loop DPD

There remains ambiguity on the practical implementation of the TOR architecture and whether or not it is necessary to have it. Open-loop DPD would be similar to factory calibration and would need to only be done once. This is, however, still unclear if it can be accomplished and further work on the thermal effect of the array on the DPD and the stability of the DPD coefficients has to be conducted. In the closed-loop implementation, the DPD feedback path architecture issue is still unsolved. The implementation of couplers at the PA output is not a feasible solution at mm-wave frequencies as it requires added design complexity and cost. A possible implementation of the TOR being considered uses near-field probing and could be potentially implemented in the sub-arrays.

EVM reduction focused DPD

The DPD solutions proposed in the literature are usually based on sub-6 GHz theory and aim to reduce the out-of-band distortions via improving the ACPR. However, ACPR is less of an issue at mm-wave frequencies and hence solutions that focus on improving the EVM, similar to the proposed generalized DPD scheme is chapter 4, have to be investigated

Real-time implementation

Lastly, if closed-loop DPD is to be implemented, the DPD training and execution must be implemented in real time. There is still much work to be done on the efficient implementation of the DPD function on real hardware and on the system learning time.

References

[1] K. Hausmair, P. N. Landin, U. Gustavsson, C. Fager, and T. Eriksson, "Digital predistortion for multi-antenna transmitters affected by antenna crosstalk," *IEEE Transactions on Microwave Theory and Techniques*, vol. 66, no. 3, pp. 1524–1535, 2017.

[2] C. Yu, L. Guan, E. Zhu, and A. Zhu, "Band-limited volterra series-based digital predistortion for wideband rf power amplifiers," *IEEE Transactions on Microwave Theory and Techniques*, vol. 60, no. 12, pp. 4198–4208, 2012.

[3] S. Bensmida, O. Hammi, A. Kwan, M. S. Sharawi, K. A. Morris, and F. M. Ghannouchi, "Extending the characterization bandwidth of dynamic nonlinear transmitters with application to digital predistortion," *IEEE Transactions on Microwave Theory and Techniques*, vol. 64, no. 8, pp. 2640–2651, 2016.

[4] H. Wang, G. Li, C. Zhou, W. Tao, F. Liu, and A. Zhu, "1-bit observation for direct-learning-based digital predistortion of rf power amplifiers," *IEEE Transactions on Microwave Theory and Techniques*, vol. 65, no. 7, pp. 2465–2475, 2017.

[5] E. Ng, Y. Beltagy, P. Mitran, and S. Boumaiza, "Single-input single-output digital predistortion of power amplifier arrays in millimeter wave rf beamforming transmitters," in *2018 IEEE/MTT-S International Microwave Symposium-IMS*. IEEE, 2018, pp. 481–484.

[6] [Online]. Available: https://www.seagate.com/files/www-content/our-story/trends/files/idc-seagate-dataage-whitepaper.pdf

[7] "Cisco visual networking index: Forecast and trends, 20172022 white paper," Feb 2019. [Online]. Available: https://www.cisco.com/c/en/us/solutions/collateral/service-provider/visual-networking-index-vni/white-paper-c11-741490.html#_Toc532256809

[8] V. Raghavan and J. Li, "Evolution of physical-layer communications research in the post-5g era," *IEEE Access*, vol. 7, pp. 10 392–10 401, 2019.

[9] H. Kato and T. Furukawa, "Two-dimensional type-preserving circular windows," *IEEE Transactions on Acoustics, Speech, and Signal Processing*, vol. 29, no. 4, pp. 926–928, 1981.

[10] T.-H. Yu and S. Mitra, "A new two-dimensional window," *IEEE transactions on acoustics, speech, and signal processing*, vol. 33, no. 4, pp. 1058–1061, 1985.

[11] V. Raghavan and J. Li, "Deembedding static nonlinearities and accurately identifying and modeling memory effects in wide-band rf transmitters," *IEEE Access*, vol. 7, pp. 10 392–10 401, 2019.

[12] T. Liu, S. Boumaiza, and F. M. Ghannouchi, "Deembedding static nonlinearities and accurately identifying and modeling memory effects in wide-band rf transmitters," *IEEE transactions on microwave theory and techniques*, vol. 53, no. 11, pp. 3578–3587, 2005.

[13] P. Singerl, A. Agrawal, A. Garg, G. Kubin, H. Eul *et al.*, "Complex baseband predistorters for nonlinear wideband rf power amplifiers," in *2006 49th IEEE International Midwest Symposium on Circuits and Systems*, vol. 2. IEEE, 2006, pp. 675–678.

[14] K. Hausmair, S. Gustafsson, C. Sánchez-Pérez, P. N. Landin, U. Gustavsson, T. Eriksson, and C. Fager, "Prediction of nonlinear distortion in wideband active antenna arrays," *IEEE Transactions on Microwave Theory and Techniques*, vol. 65, no. 11, pp. 4550–4563, 2017.

[15] G. Z. El Nashef, F. Torres, S. Mons, T. Reveyrand, T. Monédière, E. Ngoya, and R. Quéré, "Em/circuit mixed simulation technique for an active antenna," *IEEE Antennas and Wireless Propagation Letters*, vol. 10, pp. 354–357, 2011.

[16] F. M. Barradas, P. M. Tomé, J. M. Gomes, T. R. Cunha, P. M. Cabral, and J. C. Pedro, "Power, linearity, and efficiency prediction for mimo arrays with antenna coupling," *IEEE Transactions on Microwave Theory and Techniques*, vol. 65, no. 12, pp. 5284–5297, 2017.

[17] H. Yan and D. Cabric, "Digital predistortion for hybrid precoding architecture in millimeter-wave massive mimo systems," in *2017 IEEE International Conference on Acoustics, Speech and Signal Processing (ICASSP)*. IEEE, 2017, pp. 3479–3483.

[18] N. Tervo, J. Aikio, T. Tuovinen, T. Rahkonen, and A. Parssinen, "Digital predistortion of amplitude varying phased array utilising over-the-air combining," in *2017 IEEE MTT-S International Microwave Symposium (IMS)*. IEEE, 2017, pp. 1165–1168.

[19] X. Liu, Q. Zhang, W. Chen, H. Feng, L. Chen, F. M. Ghannouchi, and Z. Feng, "Beam-oriented digital predistortion for 5g massive mimo hybrid beamforming transmitters," *IEEE Transactions on Microwave Theory and Techniques*, vol. 66, no. 7, pp. 3419–3432, 2018.

[20] M. Abdelaziz, L. Anttila, A. Brihuega, F. Tufvesson, and M. Valkama, "Digital predistortion for hybrid mimo transmitters," *IEEE Journal of Selected Topics in Signal Processing*, vol. 12, no. 3, pp. 445–454, 2018.

[21] S. Deb, M. Tanio, S. Hori, N. Tawa, Y. Wada, and K. Kunihiro, "Band-limited digital predistortion with band-switching feedback architecture for 5g mmwave power amplifiers," in *2018 48th European Microwave Conference (EuMC)*. IEEE, 2018, pp. 9–12.

[22] Y. Li, J. Zhai, C. Yu, Z. Jiang, and L. Zhang, "A band-limited cpwl-based memory polynomial model for digital predistortion," in *2017 Sixth Asia-Pacific Conference on Antennas and Propagation (APCAP)*. IEEE, 2017, pp. 1–3.

[23] "Anokiwave awmf-0134 5g 28 ghz active antenna innovators kit."

[24] A. Chung, M. B. Rejeb, Y. Beltagy, A. M. Darwish, H. A. Hung, and S. Boumaiza, "Iq imbalance compensation and digital predistortion for millimeter-wave transmitters

using reduced sampling rate observations," *IEEE Transactions on Microwave Theory and Techniques*, vol. 66, no. 7, pp. 3433–3442, 2018.

[25] S. Lee, M. Kim, Y. Sirl, E.-R. Jeong, S. Hong, S. Kim, and Y. H. Lee, "Digital predistortion for power amplifiers in hybrid mimo systems with antenna subarrays," in *2015 IEEE 81st Vehicular Technology Conference (VTC Spring)*. IEEE, 2015, pp. 1–5.

[26] W. Chen, G. Lv, X. Liu, and Z. Feng, "Energy-efficient doherty power amplifier mmic and beamforming-oriented digital predistortion for 5g massive mimo application," in *2017 IEEE Asia Pacific Microwave Conference (APMC)*. IEEE, 2017, pp. 391–394.

[27] E. Ng, Y. Beltagy, G. Scarlato, A. Ben Ayed, P. Mitran, and S. Boumaiza, "Digital predistortion of millimeter-wave rf beamforming arrays using low number of steering angle-dependent coefficient sets," in *IEEE Transactions on Microwave Theory and Techniques*. IEEE, 2019, pp. 481–484.

[28] C. Yu, J. Jing, H. Shao, Z. H. Jiang, P. Yan, X.-W. Zhu, W. Hong, and A. Zhu, "Full-angle digital predistortion of 5g millimeter-wave massive mimo transmitters," *IEEE Transactions on Microwave Theory and Techniques*, vol. 67, no. 7, pp. 2847–2860, 2019.

[29] M. Romier, A. Barka, H. Aubert, J.-P. Martinaud, and M. Soiron, "Load-pull effect on radiation characteristics of active antennas," *IEEE Antennas and Wireless Propagation Letters*, vol. 7, pp. 550–552, 2008.

[30] F. M. Barradas, T. R. Cunha, and J. C. Pedro, "Digital predistortion of rf pas for mimo transmitters based on the equivalent load," in *2017 Integrated Nonlinear Microwave and Millimetre-wave Circuits Workshop (INMMiC)*. IEEE, 2017, pp. 1–4.

[31] T. Sadeghpour, R. Alhameed, N. T. Ali, I. T. Elfergani, Y. Dama, and O. O. Anoh, "Linear and nonlinear crosstalk in mimo ofdm transceivers," in *2011 18th IEEE International Conference on Electronics, Circuits, and Systems*. IEEE, 2011, pp. 504–507.

[32] "Anokiwave awmf-0128 5g 28 ghz active antenna innovators kit."

[33] Y. Liu, J. J. Yan, H.-T. Dabag, and P. M. Asbeck, "Novel technique for wideband digital predistortion of power amplifiers with an under-sampling adc," *IEEE Transactions on Microwave Theory and Techniques*, vol. 62, no. 11, pp. 2604–2617, 2014.

[34] B. A. Ahmed, E. Ng, M. Patrick, and B. Slim, "Digital predistortion of millimeter-wave hybrid beamforming transmitters using observation receivers with low-bit resolution," *Submitted to IEEE Transactions on Microwave Theory and Techniques*, 2019.

[35] D. R. Morgan, Z. Ma, J. Kim, M. G. Zierdt, and J. Pastalan, "A generalized memory polynomial model for digital predistortion of rf power amplifiers," *IEEE Transactions on signal processing*, vol. 54, no. 10, pp. 3852–3860, 2006.

[36] A. Zhu, J. C. Pedro, and T. J. Brazil, "Dynamic deviation reduction-based volterra behavioral modeling of rf power amplifiers," *IEEE Transactions on microwave theory and techniques*, vol. 54, no. 12, pp. 4323–4332, 2006.

[37] F. Mkadem, M. C. Fares, S. Boumaiza, and J. Wood, "Complexity-reduced volterra series model for power amplifier digital predistortion," *Analog Integrated Circuits and Signal Processing*, vol. 79, no. 2, pp. 331–343, 2014.